nature immunology

ARTICLES

https://doi.org/10.1038/s41590-020-00817-w

Memory-like HCV-specific CD8+ T cells retain a molecular scar after cure of chronic HCV infection

Nina Hensel[1,2,3,15], Zuguang Gu[4,15], Sagar[1,5,15], Dominik Wieland[1,2], Katharina Jechow[6], Janine Kemming[1,2,3], Sian Llewellyn-Lacey[7], Emma Gostick[7], Oezlem Sogukpinar[1,2], Florian Emmerich[2,8], David A. Price[7,9], Bertram Bengsch[1,2,10], Tobias Boettler[1,2], Christoph Neumann-Haefelin[1,2], Roland Eils[6,11], Christian Conrad[6], Ralf Bartenschlager[12,13,14], Dominic Grün[5,10], Naveed Ishaque[6,16], Robert Thimme[1,2,16] ✉ and Maike Hofmann[1,2,16] ✉

In chronic hepatitis C virus (HCV) infection, exhausted HCV-specific CD8+ T cells comprise memory-like and terminally exhausted subsets. However, little is known about the molecular profile and fate of these two subsets after the elimination of chronic antigen stimulation by direct-acting antiviral (DAA) therapy. Here, we report a progenitor–progeny relationship between memory-like and terminally exhausted HCV-specific CD8+ T cells via an intermediate subset. Single-cell transcriptomics implicated that memory-like cells are maintained and terminally exhausted cells are lost after DAA-mediated cure, resulting in a memory polarization of the overall HCV-specific CD8+ T cell response. However, an exhausted core signature of memory-like CD8+ T cells was still detectable, including, to a smaller extent, in HCV-specific CD8+ T cells targeting variant epitopes. These results identify a molecular signature of T cell exhaustion that is maintained as a chronic scar in HCV-specific CD8+ T cells even after the cessation of chronic antigen stimulation.

In the context of chronic antigen stimulation, T cell exhaustion may limit overwhelming immunopathology; however, possible consequences of restrained antigen-specific CD8+ T cell functionality are viral persistence and tumor progression[1–4]. Exhausted virus-specific CD8+ T cells are characterized by high coexpression of inhibitory receptors, altered metabolism, impaired survival, a distinct transcriptional program with an altered use of key transcription factors and an underlying unique epigenetic landscape[5–15].

Exhausted CD8+ T cells are not a homogeneous population, but rather consist of distinct subsets. In the murine lymphocytic choriomeningitis virus (LCMV) model TCF-1 and CXCR5 define progenitor/memory-like CD8+ T cells (T_{ML}) that sustain the immune response to chronic viral infection by giving rise to more dysfunctional, TCF-1$^-$PD-1^{hi}EOMES^{hi} terminally exhausted T cells (T_{TE})[16–20]. The coexistence of a less differentiated TCF-1$^+$CD127$^+$PD-1$^+$ T_{ML} and an EOMES^{hi}CD127$^-$PD-1$^+$ T_{TE} subset has also been reported in individuals chronically infected with HCV[21]. DAA-mediated cure of chronic HCV (cHCV) infection and thus antigen withdrawal led to loss of HCV-specific T_{TE} ($T_{TE/HCV}$) cells, while T_{ML} cells ($T_{ML/HCV}$) were still detectable[21]. These results not only support the central role of persisting antigen stimulation in driving terminal exhaustion but also highlight T_{ML} cells as the primary T cell population maintaining virus-specific CD8+ T cell responses during and after chronic infection. However, only very little information is available about the transcriptional profile, trajectory and fate of T_{ML} cells during and after cessation of chronic antigen stimulation. Here, we set out to address these important questions in a well-defined cohort of individuals chronically infected with HCV undergoing DAA therapy.

Results

HCV-specific CD8+ T cell diversification. Acute HCV infection can either be self-limiting, resulting in spontaneously resolved HCV (rHCV), or become a cHCV infection that can be cured by DAA treatment (cured HCV). Viral escape mutations frequently occur within HCV epitopes targeted by CD8+ T cells leading to diminished or even abrogated recognition. Both the course of infection and the emergence of viral sequence mutations impact the virus-specific CD8+ T cell response[21–28]. To analyze whether the emergence of $T_{ML/HCV}$ cells is associated with the course of HCV infection and ongoing antigen recognition (Fig. 1a), we compared the frequency of $T_{ML/HCV}$ cells in individuals with cHCV (all infected with HCV genotype 1 and non-cirrhotic), cured HCV (all after successful DAA treatment and non-cirrhotic) and rHCV. The presence of consensus versus variant viral sequences in the tested CD8+ T cell epitopes was assessed in sera of the individuals with cHCV (Supplementary Table 1). By CD127 and programmed cell death protein 1 (PD-1)

[1]Department of Medicine II, University Hospital Freiburg, Freiburg, Germany. [2]Faculty of Medicine, University of Freiburg, Freiburg, Germany. [3]Faculty of Biology, University of Freiburg, Freiburg, Germany. [4]Heidelberg Center for Personalised Oncology (DKFZ-HIPO), German Cancer Research Center (DKFZ), Heidelberg, Germany. [5]Max Planck Institute of Immunobiology and Epigenetics, Freiburg, Germany. [6]Charité – Universitätsmedizin Berlin and Berlin Institute of Health, Digital Health Center, Berlin, Germany. [7]Division of Infection and Immunity, Cardiff University School of Medicine, Cardiff, UK. [8]Institute for Transfusion Medicine and Gene Therapy, University Medical Center, University of Freiburg, Freiburg, Germany. [9]Systems Immunity Research Institute, Cardiff University School of Medicine, Cardiff, UK. [10]Signalling Research Centres BIOSS and CIBSS, University of Freiburg, Freiburg, Germany. [11]Health Data Science Unit, Faculty of Medicine, University of Heidelberg, Heidelberg, Germany. [12]Department of Infectious Diseases, Molecular Virology, Heidelberg University, Heidelberg, Germany. [13]Division Virus-Associated Carcinogenesis, German Cancer Research Center, Heidelberg, Germany. [14]German Center for Infection Research (DZIF), partner site Heidelberg, Heidelberg, Germany. [15]These authors contributed equally: Nina Hensel, Zuguang Gu, Sagar. [16]These authors jointly supervised this work: Naveed Ishaque, Robert Thimme, Maike Hofmann. ✉e-mail: robert.thimme@uniklinik-freiburg.de; maike.hofmann@uniklinik-freiburg.de

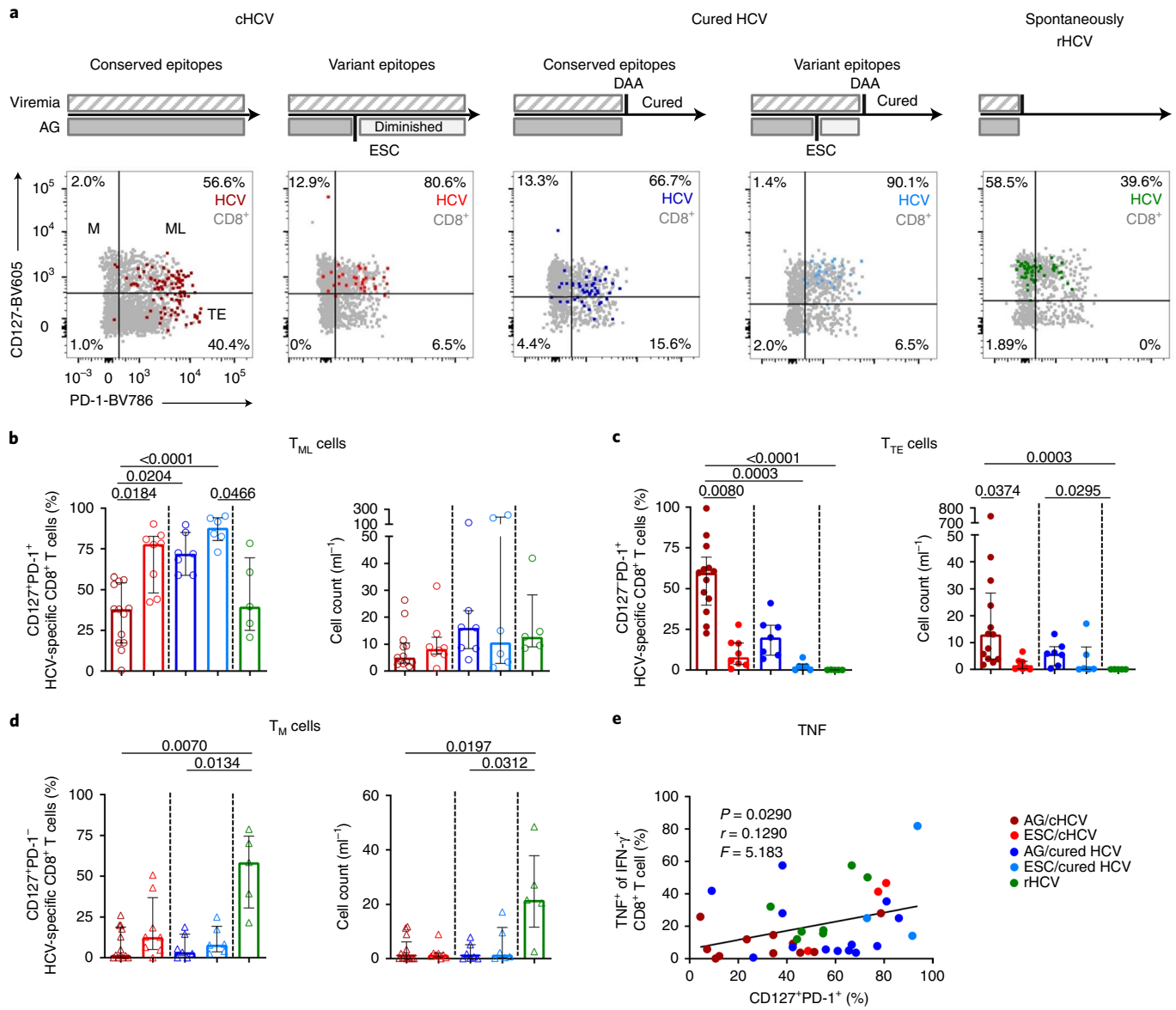

Fig. 1 | Emergence of $T_{ML/HCV}$ subsets is associated with antigen recognition. Coexpression analysis of CD127 and PD-1 of HCV-specific CD8$^+$ T cells derived from individuals with cHCV before and after DAA-mediated viral clearance (cured HCV) targeting either conserved epitopes/persisting antigen recognition (AG) or variant epitopes/diminished antigen recognition due to viral escape mutations (ESC) and after spontaneous resolution (rHCV) was analyzed. **a**, Dot plots are representative of HCV-specific (colored) and bulk (gray) CD8$^+$ T cells (M, memory; ML, memory-like; TE, terminally exhausted). **b**–**d**, Cell counts (per ml) and frequency of CD127$^+$PD-1$^+$ T_{ML} (**b**), CD127$^-$PD-1$^+$ T_{TE} (**c**) and CD127$^+$PD-1$^-$ T_M (**d**) subsets within HCV-specific CD8$^+$ T cells. **e**, Pearson correlation analysis of the frequency of TNF-producing in vitro HCV peptide-expanded CD8$^+$ IFN-γ$^+$ T cells with the abundance of CD127$^+$PD-1$^+$ T_{ML} cells among HCV-specific CD8$^+$ T cells. AG/cHCV, $n=12$ (**a**–**d**) and $n=11$ (**e**); AG/cured HCV, $n=7$ (**a**–**d**) and $n=13$ (**e**); ESC/cHCV, $n=8$ (**a**–**d**) and $n=3$ (**e**); ESC/cured HCV, $n=6$ (**a**–**d**) and $n=3$ (**e**); rHCV, $n=5$ (**a**–**d**) and $n=7$ (**e**). Bar charts show the median value with interquartile range (IQR). Statistical significance was assessed by Kruskal–Wallis test (one-sided), including Dunn's multiple-comparisons test.

coexpression analysis (Fig. 1a,b), we observed that CD127$^+$PD-1$^+$ $T_{ML/HCV}$ cells were present at highest frequencies in cured HCV versus cHCV and rHCV. In cHCV, a higher frequency of the T_{ML} cell subset was detectable among HCV-specific CD8$^+$ T cells that target variant/escaped epitopes similar to cured HCV (Fig. 1b). However, we could not detect corresponding significant differences when comparing cell counts of $T_{ML/HCV}$ subsets (Fig. 1b), indicating that the observed increase of $T_{ML/HCV}$ cells when antigen recognition is diminished is most probably not due to a strong numerical expansion. A high frequency and cell count of the T_{TE} cell subset was only present within HCV-specific CD8$^+$ T cell populations that target conserved epitopes in cHCV and thus linked to persisting antigen recognition (Fig. 1c). Classical memory CD127$^+$PD-1$^-$ HCV-specific CD8$^+$ T ($T_{M/HCV}$) cells were clearly associated with rHCV (Fig. 1d). We also tested the relevance of the $T_{ML/HCV}$ subset with respect to T cell functionality. Correlation analysis revealed that the frequency of CD127$^+$PD-1$^+$ $T_{ML/HCV}$ cells was associated with the peptide-specific production of tumor necrosis factor (TNF) by interferon (IFN)-γ$^+$ HCV-specific CD8$^+$ T cells (Fig. 1e). Thus, antigen recognition drives HCV-specific CD8$^+$ T cell diversification into T_{ML} and T_{TE} subsets relevant for functional properties of the T cell response.

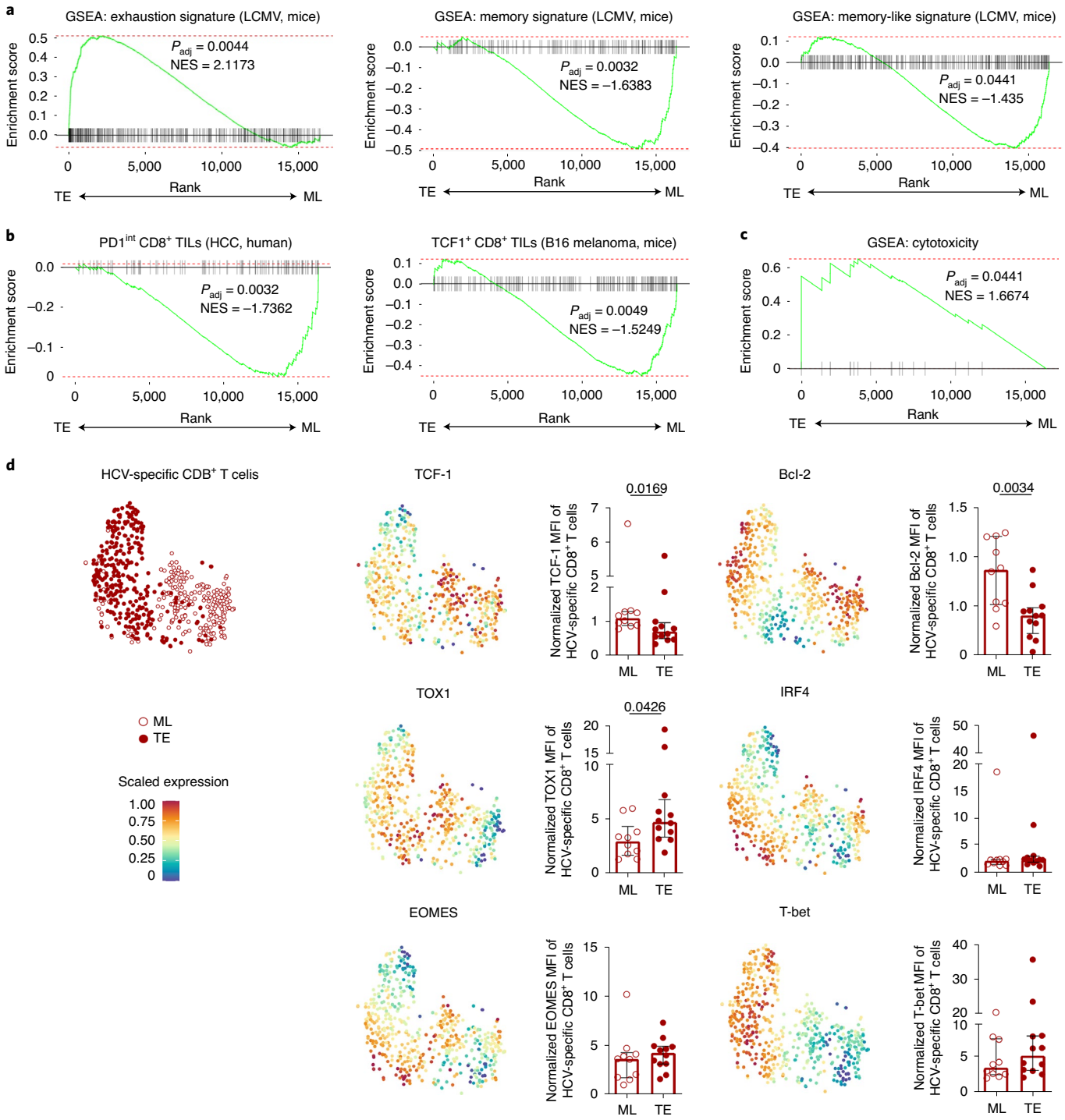

Fig. 2 | $T_{ML/HCV}$ and $T_{TE/HCV}$ cells are transcriptionally distinct. Low-input transcriptome analysis of CD127$^+$PD-1$^+$ $T_{ML/HCV}$ and CD127$^-$PD-1$^+$ $T_{TE/HCV}$ subsets (targeting conserved epitopes) derived from three individuals infected with cHCV. **a**–**c**, GSEA of exhaustion, memory and memory-like signature genes identified in the LCMV model system (**a**) and of genes associated with PD-1^{int} or TCF-1$^+$ CD8$^+$ TILs from individuals with HCC or B16 melanoma in mice, respectively (**b**), and of genes associated with cytotoxicity (**c**). **d**, *t*-SNE representation of flow cytometric data comparing $T_{ML/HCV}$ and $T_{TE/HCV}$ subsets derived from 12 individuals infected with cHCV. Scaled expression levels are color coded (red, high; blue, low). Bar charts summarizing manually gated flow cytometric data depict median fluorescence intensity (MFI) of marker expression for HCV-specific CD8$^+$ T cell subsets normalized to naive CD8$^+$ T cells. Bar charts show the median value with IQR. Significance was assessed by Mann–Whitney comparison test (two-sided). GSEA was performed using the fgsea package by taking the $\log_2$ fold change (FC) value to rank genes (one-sided).

Transcriptionally distinct HCV-specific CD8$^+$ T cells. Next, to better determine the molecular profiles of $T_{ML/HCV}$ cells during cHCV, we performed low-input transcriptome analysis. HCV-specific CD8$^+$ T cells obtained from three individuals with cHCV (Supplementary Table 1) were sorted by flow cytometry based on their CD127 and PD-1 expression, and about 100 cells each of the CD127$^+$PD-1$^+$ and

corresponding CD127$^-$PD-1$^+$ subsets were further processed for RNA sequencing (Extended Data Fig. 1). We found that 137 genes were differentially expressed (adjusted P value < 0.05) between these two subsets, including *FASLG*, *PRDM5* and *TGFB3* (Extended Data Fig. 2a). Gene-set enrichment analysis (GSEA) revealed that the CD127$^-$PD-1$^+$ T_{TE} subset was enriched for an exhausted gene expression signature (Fig. 2a), similar to those reported to be characteristic for exhausted LCMV-specific CD8$^+$ T cells, and depleted for genes associated with LCMV-specific memory CD8$^+$ T cells[19]. In contrast, CD127$^+$PD-1$^+$ $T_{ML/HCV}$ cells were enriched for (1) memory and memory-like-associated genes that have been previously identified in LCMV-specific CD8$^+$ T cells in mice (Fig. 2a)[19] and (2) genes associated with progenitor-exhausted tumor-infiltrating lymphocytes (TILs) in human hepatocellular carcinoma (HCC)[29] and in murine melanoma[30] (Fig. 2b). Thus, the CD127$^-$PD-1$^+$ $T_{TE/HCV}$ subset shares transcriptional characteristics of terminal exhaustion, while CD127$^+$PD-1$^+$ $T_{ML/HCV}$ cells also exhibit memory-like/progenitor characteristics. Furthermore, in comparison to CD127$^+$PD-1$^+$ $T_{ML/HCV}$ cells, CD127$^-$PD-1$^+$ $T_{TE/HCV}$ cells were enriched in cytotoxicity genes (Fig. 2c), suggesting a clear dichotomy in the functional capacity of these subsets. The differential transcriptional profile of $T_{ML/HCV}$ versus $T_{TE/HCV}$ cells was confirmed at the protein level by analyzing the T cell differentiation markers T-bet and EOMES, typical memory markers such as TCF-1, Bcl-2 and CCR7 and exhaustion/effector markers such as TOX1, CD39, CD38, CD137 and IRF4 (Fig. 2d and Extended Data Fig. 2b–d). Different topographical clusters of $T_{ML/HCV}$ versus $T_{TE/HCV}$ subsets were detectable after concatenating all analyzed HCV-specific CD8$^+$ T cells from individuals with cHCV and dimensionality reduction using *t*-distributed stochastic neighbor embedding (*t*-SNE; Fig. 2d and Extended Data Fig. 2c). By manual gating, we observed that the CD127$^+$PD-1$^+$ $T_{ML/HCV}$ subset displayed a significantly higher expression of TCF-1 and Bcl-2 (Fig. 2d and Extended Data Fig. 2b,d), which are associated with a high proliferative and survival capacity. In contrast, CD127$^-$PD-1$^+$ $T_{TE/HCV}$ cells showed higher expression of TOX1 and CD38 (Fig. 2d and Extended Data Fig. 2b,d), indicating both exhaustion and activation by ongoing antigen stimulation. To further assess the relationship of $T_{ML/HCV}$ and $T_{TE/HCV}$ cells, we analyzed the T cell antigen receptor (TCR) clonotypes within the respective subsets via complementarity-determining region 3 (CDR3) sequences. A representative overview of the TCR clonotype distribution within $T_{ML/HCV}$ and $T_{TE/HCV}$ subsets obtained from one cHCV individual is depicted in three-layer donut plots in Extended Data Fig. 2e. Both subsets share some TCR clonotypes (Extended Data Fig. 2f), also suggesting possible transition/plasticity between CD127$^+$PD-1$^+$ $T_{ML/HCV}$ and CD127$^-$PD-1$^+$ $T_{TE/HCV}$ cells. In sum, transcriptional profiling revealed distinct characteristics of $T_{ML/HCV}$ and $T_{TE/HCV}$ cells, and especially a polarization of $T_{ML/HCV}$ cells towards T cell memory.

Progenitor–progeny relationship of $T_{ML/HCV}$ and $T_{TE/HCV}$ cells. To further determine the subset diversification in an unbiased approach, we performed single-cell RNA sequencing (scRNA-seq) of circulating HCV-specific CD8$^+$ T cells obtained from individuals with cHCV (Extended Data Fig. 1). Cluster analysis applying the RaceID3 algorithm[31] to single-cell transcriptomes of 784 cells from six individuals with cHCV (Supplementary Table 1) revealed the existence of three different clusters/subsets among HCV-specific CD8$^+$ T cells during cHCV (Fig. 3a). Differentially expressed genes (DEGs) among these three HCV-specific CD8$^+$ T cell clusters/subsets included *CCL4*, *CCL5*, *GZMA*, *GZMK*, *IL7R* and *TCF7* and thus covering migratory, functional, homeostatic and proliferative characteristics (Fig. 3a). Pearson correlation showed that clusters/subsets 1 and 3 were most different and clusters/subsets 1 and 2 showed more overlap and similarities with each other compared to clusters/subsets 2 and 3 (Fig. 3b). Diffusion pseudotime (DPT) analysis[32] of HCV-specific CD8$^+$ T cells revealed that the three clusters/subsets were residing on a one-dimensional manifold reflecting a continuous dynamic process without branching (Fig. 3c), suggesting a progenitor–progeny relationship of cluster/subset 1 to cluster/subset 3 via the intermediate cluster/subset 2. In particular, transcripts of *TNFRSF9* (encoding CD137), *CD38* and *IRF4*, all associated with T cell activation, increased during this process; while transcripts of *IL7R* and *TCF7*, all required for T cell homeostasis, decreased during this process (Fig. 3c and Extended Data Fig. 3a). Cluster/subset 1 was enriched in signature genes of T cell memory[19] and cluster/subset 3 in signature genes of exhausted CD8$^+$ T cells[19], whereas the gene signature of cluster/subset 2 was in between (Fig. 3d). Thus, cluster/subset 1 most likely represents $T_{ML/HCV}$ cells that differentiate via cluster/subset 2, an intermediate stage, into $T_{TE/HCV}$ cells of cluster/subset 3. To validate these data, we analyzed whether the differential *IL7R* (encoding CD127) transcript abundance could be confirmed by expression of the CD127 protein. Indeed, three discrete CD127^{lo}, CD127^{int} and CD127^{hi} HCV-specific CD8$^+$ T cell subsets (Fig. 3e) with differential expression patterns of memory (TCF-1, Bcl-2 and CCR7) and exhaustion/effector (TOX1, PD-1, CD39, CD38, CD137 and IRF4) markers (Fig. 3f,g and Extended Data Fig. 3b) were detectable by flow cytometry. Furthermore, diffusion maps generated from the flow cytometry data confirmed the continuous relationship of CD127^{hi}, CD127^{int} and CD127^{lo} HCV-specific CD8$^+$ T cells, similar to the DPT analysis of the scRNA-seq data (Fig. 3g). In summary, scRNA-seq analysis not only confirmed the existence of a CD127^{hi} $T_{ML/HCV}$ subset but also uncovered the presence of three HCV-specific CD8$^+$ T cell subsets in cHCV that are in a progenitor–progeny relationship via a discrete CD127^{int} intermediate stage.

The molecular scar of HCV-specific CD8$^+$ T cells. Next, we assessed whether the exhausted profile of HCV-specific CD8$^+$

Fig. 3 | Progenitor–progeny relationship of $T_{ML/HCV}$ and $T_{TE/HCV}$ cells. scRNA-seq of 784 HCV-specific CD8$^+$ T cells from six individuals infected with cHCV. **a**, Cluster analysis via RaceID3 algorithm applied to single-cell transcriptomes. Plot represents a *k*-nearest neighbor graph layout utilizing the Fruchterman–Rheingold algorithm. Each dot corresponds to one individual cell. Three clusters were identified and color coded. Bubble plot of DEGs among the three clusters is displayed. The fraction scale is depicted from 0 to 1. **b**, Analysis of transcriptional similarity between clusters 1–3 by Pearson correlation. **c**, DPT trajectory of clusters 1–3. Each dot represents one cell. Its location indicates the cell's stage in the cluster 1-to-cluster 3 transition (top). Self-organizing map (SOM) of *z*-score-transformed pseudotemporal expression profiles along the cluster 1-to-cluster 3 transition. The color coding at the bottom indicates the cluster of origin. The SOM identified 17 different modules of coregulated genes (middle). Expression levels of representative genes in pseudotime are shown (bottom). **d**, Comparison of clusters 1–3 by investigation of exhausted and memory signature gene sets (identified in the murine LCMV model system). Violin plots depict the aggregated transcript counts. **e**, mRNA expression level of *IL7R* in the three clusters and flow cytometric analysis of the CD127 expression on HCV-specific CD8$^+$ T cells derived from individuals infected with cHCV (mRNA, $n = 6$; flow cytometry, $n = 12$). Exemplary histograms and dot plot (plotted against side scatter area (SSC-A)), frequencies and cell counts (per ml) of CD127 subsets (CD127^{lo}, CD127^{int} and CD127^{hi}) are depicted. **f**,**g**, Diffusion maps used for dimensional reduction of flow cytometric data combining various T cell memory and exhaustion/effector markers expressed by CD127^{lo}, CD127^{int} and CD127^{hi} HCV-specific CD8$^+$ T cell subsets derived from twelve individuals infected with HCV. Scaled expression levels are color coded (red, high; blue, low). Statistical significance was assessed by Kruskal–Wallis test (one-sided), including Dunn's multiple-comparisons test for flow cytometric analysis and Wilcoxon matched-pairs signed-rank test (two-sided) for violin plots of mRNA expression levels. The violin plots show the frequency, with box plots depicting the median value with IQR.

T cells is reversed after cessation of long-term persisting antigen recognition. We concatenated all flow cytometry-analyzed HCV-specific CD8⁺ T cells from participants before and after HCV cure and in rHCV (Supplementary Table 1) by *t*-SNE (Fig. 4a and Extended Data Fig. 4a). HCV-specific CD8⁺ T cells from cHCV versus cured HCV versus rHCV showed distinct topographical clustering, while HCV-specific CD8⁺ T cells after HCV cure were characterized by a cluster of markers overlapping with those expressed by HCV-specific CD8⁺ T cells from rHCV (for example, TCF-1 and Bcl-2) and cHCV (for example, TOX1 and EOMES; Fig. 4a and Extended Data Fig. 4a,b). This observation indicates at least a partial repolarization from T cell exhaustion/activation towards T cell memory within the overall HCV-specific CD8⁺ T cell populations, while marker molecules characteristic for T cell exhaustion like TOX1 were still elevated after HCV cure compared to rHCV. In agreement with a previous study from our group[21], HCV cure was accompanied by an increased frequency of CD127⁺PD-1⁺ $T_{ML/HCV}$ cells (Extended Data Fig. 4c). Thus, HCV-specific CD8⁺

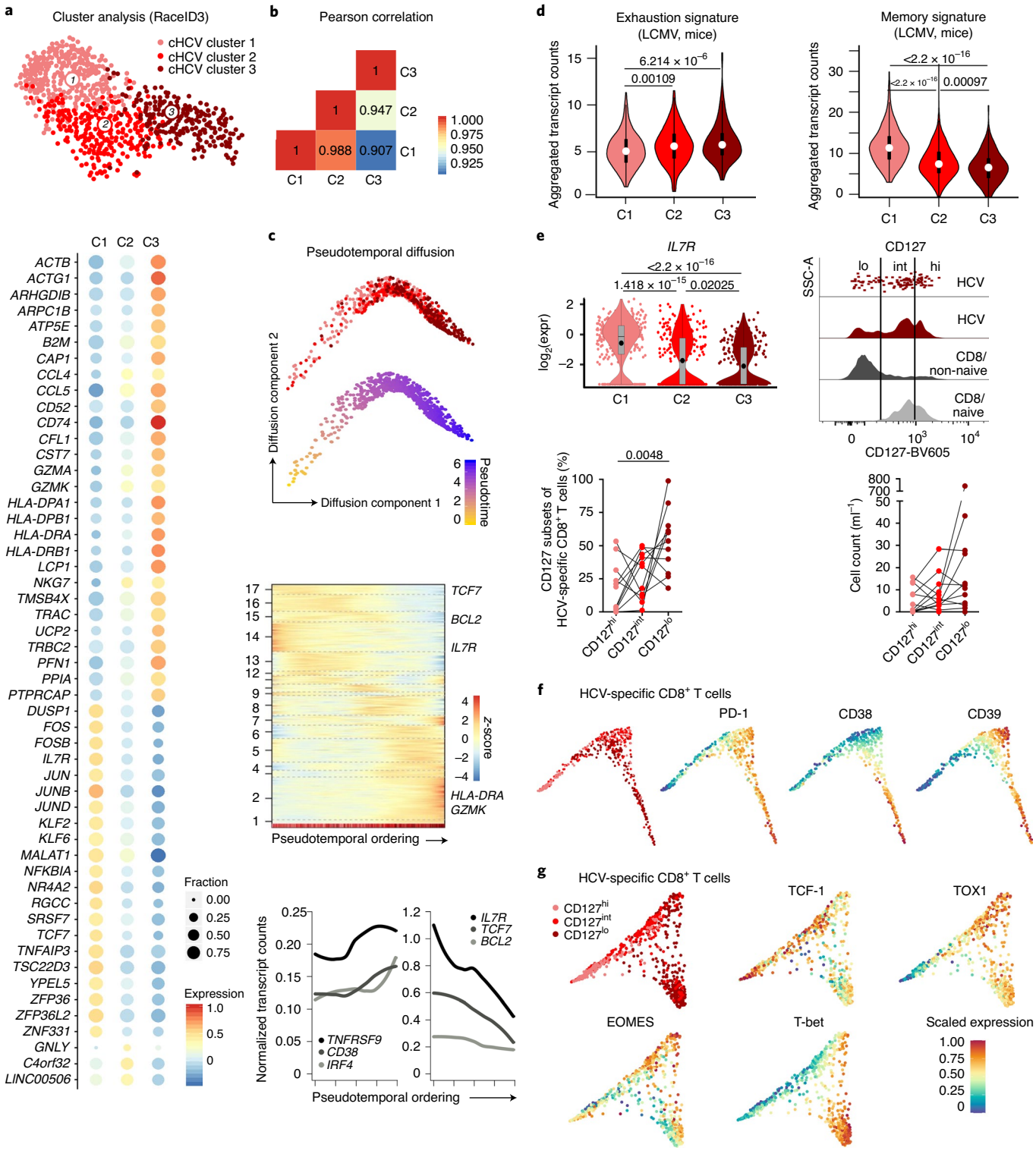

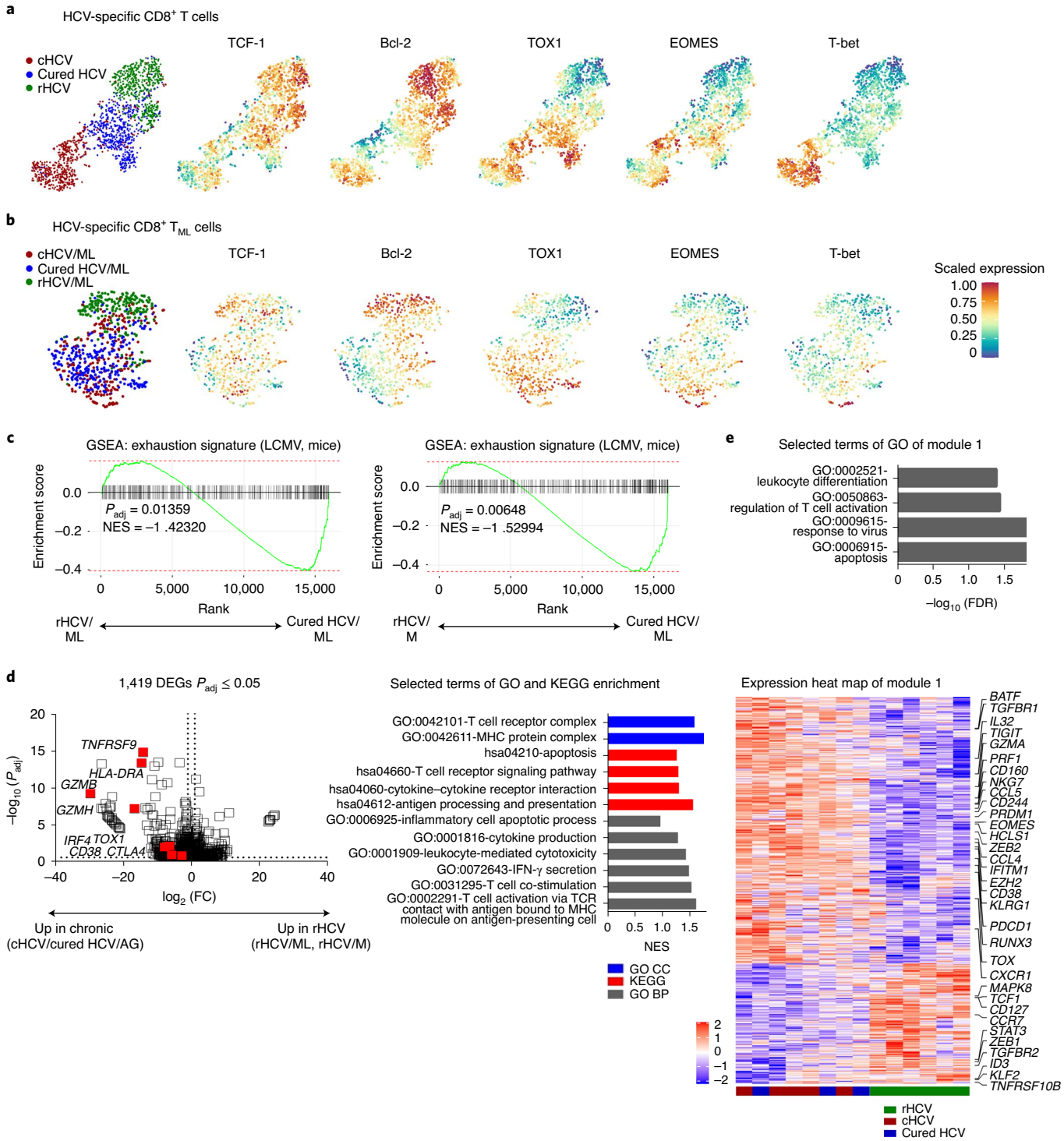

Fig. 4 | The molecular scar of chronicity after HCV cure. a,**b**, *t*-SNE representation of flow cytometric data including various T cell memory and exhaustion/effector markers comparing HCV-specific CD8⁺ T cells (**a**) and $T_{ML/HCV}$ cells (**b**) in cHCV ($n=12$), cured HCV ($n=7$) or rHCV ($n=5$). Scaled expression levels are color coded (red, high; blue, low). **c**, GSEA of exhaustion signature genes (identified in the LCMV mouse model) comparing low-input transcriptome data of CD127⁺PD-1⁺ $T_{ML/HCV}$ cells after HCV cure and CD127⁺PD-1⁺ (left) or CD127⁺PD-1⁻ memory (right) subsets in rHCV (cured HCV and rHCV, $n=3$ each). **d**, Volcano plot showing DEGs (low-input transcriptome data) of $T_{ML/HCV}$ subsets before and after HCV cure and memory subsets in rHCV (red, exemplary DEGs are specified) (cHCV, cured HCV and rHCV, $n=3$ each). The *x* axis represents the $\log_2$ FC, and the *y* axis represents the $-\log_{10}$ adjusted *P* values ($P_{adj} \leq 0.05$). The dotted lines indicate filter criteria: $\log_2$ FC of ±1 and adjusted *P* value of 0.05. Gene ontology (GO) and Kyoto Encyclopedia of Genes and Genomes (KEGG) pathway enrichment analysis of the DEGs. BP, biological process; CC, cellular components; MHC, major histocompatibility complex; NES, normalized enrichment score. **e**, Coexpression network analysis of low-input transcriptome data was performed using WGCNA. GO enrichment analysis was performed for module 1, and gene expression analysis of module 1 is depicted as a heat map. GSEA was performed by the fgsea package by taking $\log_2$ FC to rank genes (one-sided). DEG analysis of the volcano plot (two-sided) was performed with DESeq2. All *P* values were corrected by the Benjamini–Hochberg method. GO and KEGG enrichment on significant DEGs were performed by clusterProfiler (one-sided). FDR, false discovery rate.

T cells detectable after HCV cure are predominantly within the T_{ML} subset. Based on these observations, we asked whether CD127$^+$PD-1$^+$ $T_{ML/HCV}$ cells display differential transcriptional and phenotypic characteristics during chronic infection, after cure or spontaneous resolution, for example, whether they also repolarize towards bona fide T cell memory after HCV cure. *t*-SNE analysis displayed that $T_{ML/HCV}$ cells from cHCV and after HCV cure intermingled and clearly separated from $T_{M/HCV}$ cells from rHCV (Fig. 4b and Extended Data Fig. 5a). As confirmed by manual gating, the only significant difference between $T_{ML/HCV}$ cells before and after HCV cure was CD38 expression that was reduced after HCV cure and most likely indicates diminished antigen stimulation (Extended Data Fig. 5b). TOX1, PD-1, Bcl-2 and CCR7 expression levels were similar in $T_{ML/HCV}$ cells at the end of DAA treatment and at long-term follow-up time points after HCV cure (Extended Data Fig. 6a). Principle-component analysis of low-input RNA-seq-generated transcriptomes of $T_{ML/HCV}$ subsets before and after HCV cure and in rHCV, as well as of $T_{TE/HCV}$ and $T_{M/HCV}$ cells, also revealed that the CD127$^+$PD-1$^+$ $T_{ML/HCV}$ subset after HCV cure did not cluster with HCV-specific CD8$^+$ T cells after spontaneous resolution and thus with bona fide memory T cells (Extended Data Fig. 6b). GSEA further revealed that, in comparison to CD127$^+$PD-1$^+$ and CD127$^+$PD-1$^-$ subsets in rHCV, $T_{ML/HCV}$ cells after HCV cure were enriched for signature genes of T cell exhaustion (Fig. 4c). These results suggest that the molecular program of T cell exhaustion obtained during cHCV infection is maintained in $T_{ML/HCV}$ cells even after DAA-mediated cure. Thus, $T_{ML/HCV}$ cells exhibit a molecular scar of chronicity after HCV cure. The differences in the molecular program of HCV-specific CD8$^+$ T cells in rHCV versus cHCV/cured HCV were reflected by 1,419 DEGs that were enriched for gene sets associated with T cell activation and thus covering essential processes in T cell biology (Fig. 4d). These results point towards differences in essential T cell processes in HCV-specific CD8$^+$ T cell subsets in cHCV/cured HCV versus rHCV. Weighted gene coexpression network analysis (WGCNA) of low-input RNA-seq data further showed that central regulatory networks like module 1 (Extended Data Fig. 6c), which include genes orchestrating leukocyte differentiation, apoptosis, T cell activation and antiviral immune responses (for example, *TOX1*, *EOMES*, *RUNX3* and *BATF*), are different in HCV-specific CD8$^+$ T cell subsets associated with HCV chronicity compared to spontaneous resolution (Fig. 4e). Taken together, even after HCV cure, $T_{ML/HCV}$ cells display a chronic scar that reflects a molecular program associated with T cell exhaustion.

$T_{ML/HCV}$ cells retain the molecular scar after HCV cure. To further analyze the fate of $T_{ML/HCV}$ cells after HCV cure, we performed scRNA-seq analyses of HCV-specific CD8$^+$ T cells that were longitudinally sampled before and after HCV cure (Extended Data Fig. 1 and Supplementary Table 1). In agreement with our previous findings, three different HCV-specific CD8$^+$ T cell cluster/subsets could be defined by RaceID3 cluster analysis[31] of single-cell transcriptomes of approximately 200 cells each from two individuals with cHCV before and after HCV cure, complemented by cells from four additional individuals with cHCV without treatment (Fig. 5a). These results indicate that HCV cure does not induce new HCV-specific CD8$^+$ T cell clusters/subsets compared to established cHCV, but rather reduces the heterogeneity of HCV-specific CD8$^+$ T cells. Indeed, in contrast to the presence of three defined HCV-specific CD8$^+$ T cell clusters/subsets present before initiation of DAA therapy, HCV-specific CD8$^+$ T cells after HCV cure lacked cluster/subset 3 and were primarily distributed to cluster/subset 1, and to a minor fraction to cluster/subset 2 (Fig. 5a). Since cluster/subset 3 was enriched in signature genes of terminal T cell exhaustion, these results suggest that the reduced heterogeneity of HCV-specific CD8$^+$ T cells is primarily caused by loss of terminally exhausted cells after HCV cure (Fig. 5b). The three clusters/subsets can be discriminated by *IL7R*/CD127 mRNA and protein expression (Fig. 5c). Comparison of HCV-specific CD8$^+$ T cells in clusters/subsets 1 and 2 revealed a low number of DEGs before and after HCV cure thus indicating a high degree of similarity between these cells (Fig. 5d). This observation was confirmed by quadratic programming, which represents a measure of similarity (Fig. 5e). In addition, phenotypic analysis, including TCF-1, Bcl-2, CCR7, TOX1, PD-1, CD39, CD38, CD137 and IRF4, revealed that there was hardly any difference between HCV-specific CD8$^+$ T cells from subset 1 (CD127^{hi}) and subset 2 (CD127^{int}) before and after HCV cure (Fig. 5f and Extended Data Fig. 7a–c). The only exception was CD38 expression on CD127^{int} HCV-specific CD8$^+$ T cells of subset 2 that was reduced after HCV cure (Extended Data Fig. 7a). Thus, these data clearly suggest that CD127^{hi} and CD127^{int} HCV-specific CD8$^+$ T cells are T_{ML} subsets that are maintained after HCV cure. Next, we addressed the clonal relationship of $T_{ML/HCV}$ cells before and after HCV cure via CDR3 sequences to determine maintenance of distinct $T_{ML/HCV}$ cell clones (Fig. 5g). In a longitudinal analysis, we found some T cell clones that were detectable within the $T_{ML/HCV}$ cell population before and after HCV cure, while others were unique for the respective T cell population. In sum, $T_{ML/HCV}$ subsets before and after HCV cure share a high degree of similarity including

Fig. 5 | $T_{ML/HCV}$ cells retain the chronic scar after HCV cure. scRNA-seq of 1,081 HCV-specific CD8$^+$ T cells in cHCV ($n=6$) and cured HCV ($n=2$). **a**, Cluster analysis via RaceID3 algorithm. Each dot corresponds to one individual cell. Clusters (1–3; defined in Fig. 3a) are color coded (gray, HCV-specific CD8$^+$ T cells in cured HCV) and the proportion of HCV-specific CD8$^+$ T cells before and after HCV cure was assessed for each cluster. **b**, Comparison of clusters 1–3 (including HCV-specific CD8$^+$ T cells before and after HCV cure) by investigation of exhausted and memory signature genes. Violin plots depict the aggregated transcript counts. **c**, Single-cell mRNA expression of *IL7R* illustrated in the Fruchterman–Rheingold algorithm representation. Transcript levels are color coded. For flow cytometric analysis, exemplary histograms and dot plot (plotted against SSC-A), frequencies and cell counts (per ml) of CD127 subsets (CD127^{lo}, CD127^{int} and CD127^{hi} representing clusters 1–3) of HCV-specific CD8$^+$ T cells from participants before ($n=12$) and after ($n=7$) HCV cure are depicted. **d**, Volcano plot showing DEGs from clusters 1 and 2 of HCV-specific CD8$^+$ T cells from participants before and after cure (red, exemplary DEGs are specified). The *x* axis represents the $\log_2$ FC, and the *y* axis represents the $-\log_{10}$ adjusted *P* values (≤ 0.05). Dotted lines indicate filter criteria of $\log_2$FC ± 1 and adjusted *P* value of 0.05. **e**, Fruchterman–Rheingold algorithm representation of cHCV dataset showing the weights for HCV-specific CD8$^+$ T cells after HCV cure calculated using quadratic programming. Color scale represents weights on the scale of 0 to 1. **f**, Flow cytometric analysis of TCF-1 and TOX1 (depicted as MFI normalized to naive CD8$^+$ T cells) in CD127^{int} and CD127^{hi} (representing clusters 1 and 2) HCV-specific CD8$^+$ T cells from participants before ($n=12$) and after ($n=7$) HCV cure. **g**, Comparison of TCR clonotypes (low-input transcriptome analysis) of $T_{ML/HCV}$ subsets from participants before ($n=3$) and after ($n=3$) HCV cure by CDR3 sequences. Representative overview of the TCR clonotype distribution from one individual (of three) with cHCV before and after cure is depicted in three-layer donut plots: the inner layer depicts singleton, doubleton and high-order clonotypes; the second layer displays the top percentiles of clonotypes from the higher-order clonotypes; and the outer layer displays individual abundances of the most recurrent clonotypes. Clonal overlap was assessed. Bar charts show the median value with IQR. Statistical significance of flow cytometric analysis and TCR clonotypes was assessed by Kruskal–Wallis test (one-sided), including Dunn's multiple-comparisons test and Wilcoxon matched-pairs signed-rank test (two-sided) for violin plots. The violin plots show the frequency, and box plots depict the median value with IQR. Differential gene expression analysis was performed using the diffexpnb function of the RaceID3 algorithm.

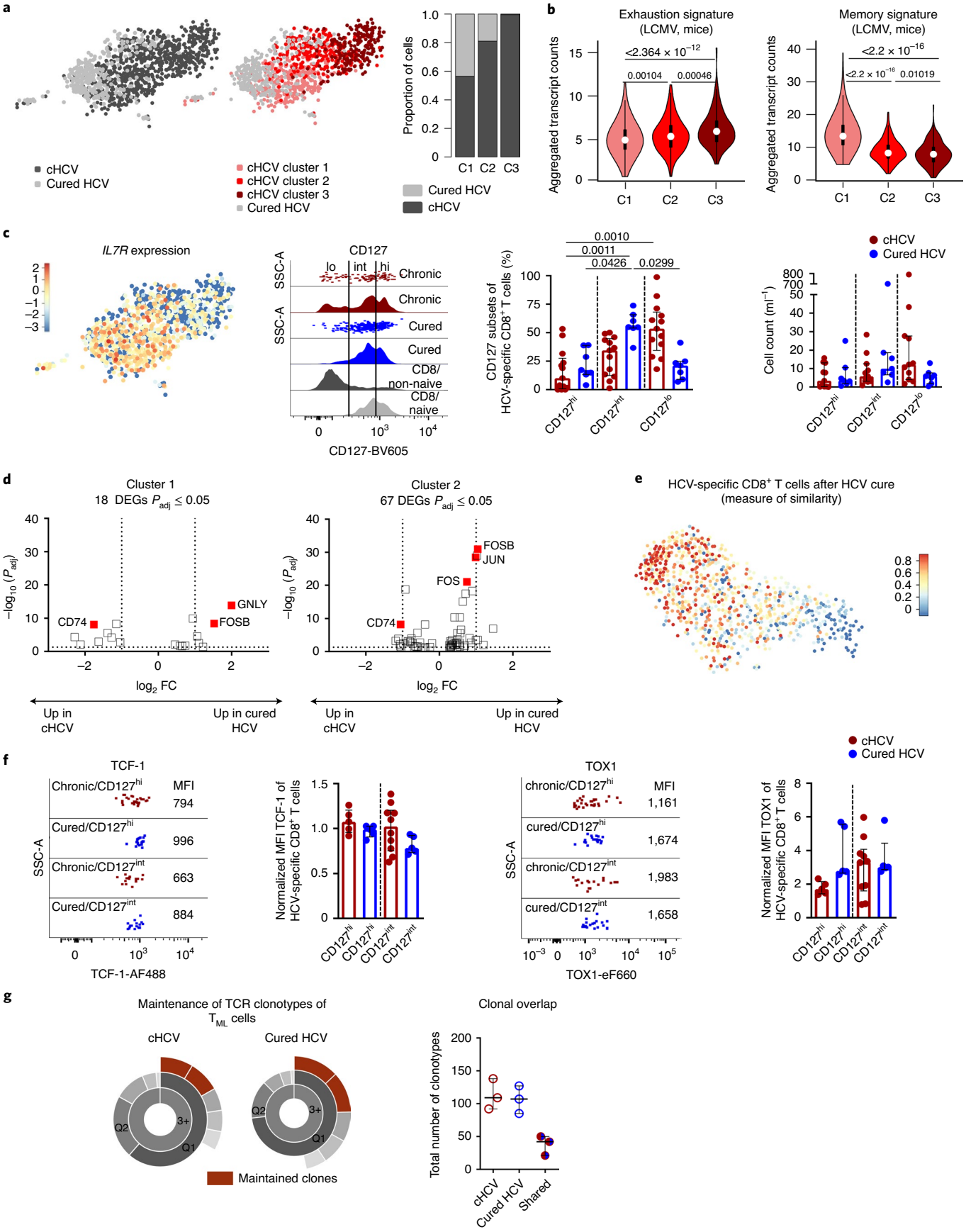
a
cHCV
Cured HCV
cHCV cluster 1
cHCV cluster 2
cHCV cluster 3
Cured HCV
Proportion of cells
C1 C2 C3
Cured HCV
cHCV
b
Exhaustion signature (LCMV, mice)
Memory signature (LCMV, mice)
Aggregated transcript counts
<2.364 × 10−12
0.00104
0.00046
<2.2 × 10−16
<2.2 × 10−16
0.01019
C1 C2 C3
c
IL7R expression
CD127
lo int hi
SSC-A
Chronic
Chronic
Cured
Cured
CD8/ non-naive
CD8/ naive
CD127-BV605
CD127 subsets of HCV-specific CD8+ T cells (%)
0.0010
0.0011
0.0426
0.0299
CD127hi CD127int CD127lo
cHCV
Cured HCV
Cell count (ml−1)
d
Cluster 1
18 DEGs Padj ≤ 0.05
Cluster 2
67 DEGs Padj ≤ 0.05
−log10 (Padj)
log2 FC
CD74
GNLY
FOSB
FOS
JUN
Up in cHCV
Up in cured HCV
e
HCV-specific CD8+ T cells after HCV cure (measure of similarity)
f
TCF-1
Chronic/CD127hi MFI 794
Cured/CD127hi 996
Chronic/CD127int 663
Cured/CD127int 884
SSC-A
TCF-1-AF488
Normalized MFI TCF-1 of HCV-specific CD8+ T cells
TOX1
chronic/CD127hi MFI 1,161
cured/CD127hi 1,674
chronic/CD127int 1,983
cured/CD127int 1,658
TOX1-eF660
Normalized MFI TOX1 of HCV-specific CD8+ T cells
cHCV
Cured HCV
g
Maintenance of TCR clonotypes of TML cells
cHCV
Cured HCV
Q1
Q2
3+
Maintained clones
Clonal overlap
Total number of clonotypes
cHCV
Cured HCV
Shared

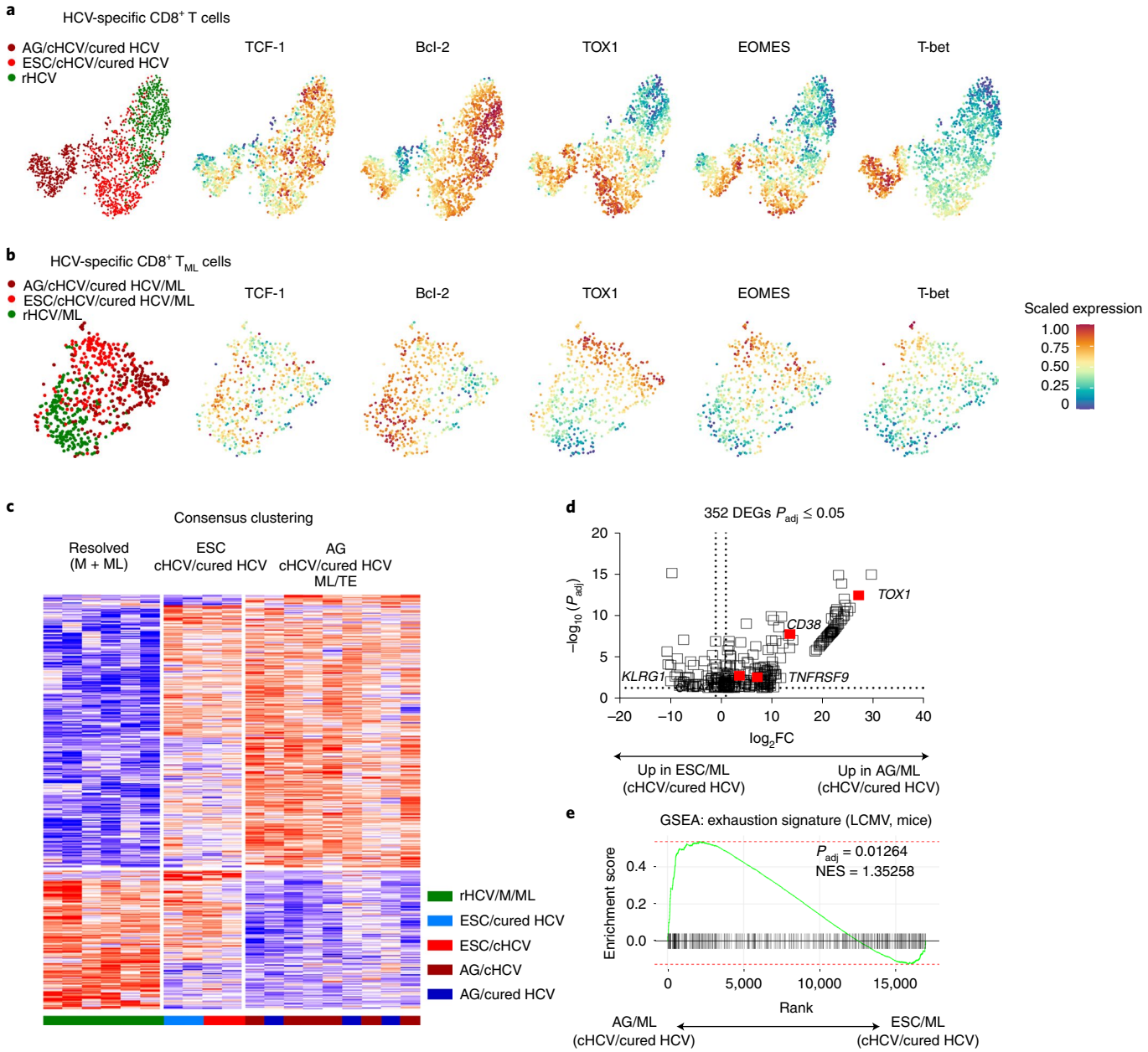

Fig. 6 | The chronic scar is determined by antigen recognition. a,**b**, *t*-SNE representation of flow cytometric data, including various T cell memory and exhaustion/effector markers of HCV-specific CD8+ T (**a**) and CD127+PD-1+ $T_{ML/HCV}$ (**b**) cells derived from individuals with rHCV ($n=5$), cHCV and cured individuals targeting either conserved epitopes (AG; cHCV, $n=12$; cured HCV, $n=7$) or variant epitopes (ESC; cHCV, $n=8$; cured HCV, $n=6$). Scaled expression levels are color coded (red, high; blue, low). **c**, Unsupervised consensus clustering between the transcriptomes of CD127/PD-1-based subsets of HCV-specific CD8+ T cells from individuals with cHCV/cured individuals with ($n=2$) or without ($n=3$) viral escape mutations, and from individuals with rHCV ($n=3$). **d**, Volcano plot showing DEGs (low-input transcriptome data) of $T_{ML/HCV}$ cells obtained from cHCV/cured HCV individuals with or without viral escape mutations (red, exemplary DEGs are specified). The *x* axis represents the $\log_2$ FC and the *y* axis represents the $-\log_{10}$ adjusted *P* values ($\leq$0.05). Dotted lines indicate filter criteria: $\log_2$FC of $\pm$1 and adjusted *P* value of 0.05. **e**, GSEA of exhaustion signature genes (identified in the LCMV mouse model) comparing $T_{ML/HCV}$ subsets from individuals with cHCV/cured individuals with or without viral escape mutations (low-input transcriptome data). GSEA was performed using the fgsea package by taking the $\log_2$ FC value to rank genes (one-sided). DEG analysis of the volcano plot (two-sided) was performed using DESeq2. All *P* values are corrected by the Benjamini–Hochberg method.

clonotypes. This suggests that $T_{ML/HCV}$ cells are maintained after viral elimination and with this retain the chronic scar in HCV-specific CD8+ T cell populations after HCV cure.

Antigen recognition determines the molecular scar. To assess the impact of antigen recognition on the establishment of the chronic scar, we analyzed HCV-specific CD8+ T cells that target variant epitopes in individuals with cHCV before and after cure. *t*-SNE analysis of flow cytometry data including TCF-1, Bcl-2, CCR7, TOX1, PD-1, CD39, CD38, CD137 and IRF4 revealed a topographically different clustering of HCV-specific CD8+ T cells targeting variant versus conserved epitopes (Fig. 6a and Extended Data Fig. 8a). HCV-specific CD8+ T cells targeting variant epitopes partially overlapped with HCV-specific CD8+ T cells from rHCV (for example,

Bcl-2 and TCF-1) and partially with HCV-specific CD8+ T cells targeting conserved epitopes (for example, TOX1, EOMES, PD-1 and CD39). Furthermore, manual gating revealed that HCV-specific CD8+ T cells that target variant versus conserved epitopes exhibited differential expression of Bcl-2, TOX1, EOMES, PD-1 and CD39 in both cHCV and cured HCV (Extended Data Fig. 8b). Of note, we did not detect differences in the analyzed markers between HCV-specific CD8+ T cells targeting variant epitopes before and after HCV cure (Extended Data Fig. 8b). These results indicate differences in the polarization towards the T cell memory and the effector/exhausted T cell fate of HCV-specific CD8+ T cells targeting conserved versus variant epitopes. To rule out the possibility that this was simply owing to the lack of the T_{TE} subset in HCV-specific CD8+ T cell populations that target variant epitopes, we also compared $T_{ML/HCV}$ cells targeting conserved compared to variant epitopes. $T_{ML/HCV}$ subsets showed distinct topographical clustering when comparing variant versus conserved epitopes in cHCV/cured HCV and spontaneous resolution similar to the overall HCV-specific CD8+ T cell population (Fig. 6b and Extended Data Fig. 9a). Manual gating confirmed statistically different expression of CCR7, PD-1 and CD39 on $T_{ML/HCV}$ cells targeting variant compared to conserved epitopes (Extended Data Fig. 9b). Thus, although $T_{ML/HCV}$ cells targeting variant compared to conserved epitopes in cHCV/cured HCV were more similar to HCV-specific CD8+ T cells detectable in rHCV infection, these cells still exhibited a distinct expression pattern of marker molecules for T cell memory and exhausted/effector T cells. By applying an unsupervised consensus clustering approach comparing the transcriptomes of CD127/PD-1-based subsets of HCV-specific CD8+ T cells in cHCV, cured HCV and rHCV that either target conserved or variant epitopes (Supplementary Table 1), we identified three different molecular signatures (Fig. 6c) associated with (1) rHCV, (2) $T_{ML/HCV}$ cells targeting variant epitopes and (3) HCV-specific CD8+ T cells targeting conserved epitopes irrespective of whether these cells were obtained before or after HCV cure. The transcriptional signature of $T_{ML/HCV}$ cells targeting variant epitopes clustered in between the other two groups. This signature of 'T cell escape' was more similar to the profile of HCV-specific CD8+ T cells targeting conserved epitopes in cHCV/cured HCV than to that of HCV-specific CD8+ T cells in rHCV, again supporting a chronic molecular scar also in $T_{ML/HCV}$ cells targeting variant epitopes. To better define the chronic scar of HCV-specific CD8+ T cells targeting variant versus conserved epitopes in cHCV/cured HCV, we performed DESeq2 analysis (Fig. 6d). We detected 352 DEGs ($P_{adj} < 0.05$), including a higher mRNA expression of *TOX1*, *KLRG1*, *CD38* and *TNFRSF9* (encoding CD137), in $T_{ML/HCV}$ cells targeting conserved compared to variant epitopes. HCV-specific CD8+ T cells targeting conserved compared to variant epitopes were enriched for genes associated with T cell exhaustion (Fig. 6e). Hence, the molecular program associated with T cell exhaustion and thus the chronic scar seems to be fortified in HCV-specific CD8+ T cells targeting conserved versus variant epitopes. To summarize, $T_{ML/HCV}$ cells targeting variant epitopes also exhibit a chronic scar, although less pronounced compared to $T_{ML/HCV}$ cells targeting conserved epitopes. Therefore, these results suggest that the chronic scar is determined by antigen recognition.

Discussion

Here, we report the existence of three different $CD127^{hi}$, $CD127^{int}$ and $CD127^{lo}$ exhausted HCV-specific CD8+ T cell subsets in long-term cHCV. $CD127^{hi}$ HCV-specific CD8+ T cells exhibit the molecular signature of previously described $CD127^{+}PD\text{-}1^{+}$ $T_{ML/HCV}$ cells[21], while $CD127^{lo}$ cells resemble T_{TE} cells. These differential molecular signatures of T_{ML} versus T_{TE} subsets are in line with studies conducted in the murine model system of chronic LCMV infection[5,12,13,15,18,19,33] and in preclinical and clinical cancer models[30,34,35]. Thus, a molecular core signature underlying exhausted CD8+ T cell heterogeneity in chronic viral infection is highly conserved between humans and mice. scRNA-seq revealed a progenitor–progeny relationship of $CD127^{hi}$ $T_{ML/HCV}$ and $CD127^{lo}$ $T_{TE/HCV}$ cells via a $CD127^{int}$ intermediate stage, which is further supported by shared TCR clones within $T_{ML/HCV}$ and $T_{TE/HCV}$ subsets. A progenitor–progeny relationship within exhausted virus-specific CD8+ T cells has been previously reported in the LCMV mouse model[12,13,18,19], but not in humans[1]. This progenitor–progeny relationship sets the basis for the observed heterogeneity of exhausted CD8+ T cells in humans and mice and ensures the maintenance of the virus-specific CD8+ T cell response during chronic viral infection.

Transcriptome profiling also showed that $T_{ML/HCV}$ cells arising during cHCV infection are indeed maintained after HCV cure. In particular, the transcriptomes of $T_{ML/HCV}$ cells present before or after HCV cure were nearly identical and they also shared many TCR clonotypes. Maintenance of $T_{ML/HCV}$ and loss of $T_{TE/HCV}$ subsets led to a memory polarization of the overall HCV-specific CD8+ T cell response. However, the overall transcriptome of $T_{ML/HCV}$ cells before and after HCV cure is clearly different compared to a bona fide HCV-specific CD8+ T cell memory detectable in rHCV. Consequently, a molecular signature of T cell exhaustion resembling a chronic scar is maintained in HCV-specific CD8+ T cells even after HCV cure that cannot simply be reversed by viral clearance. Analyses of the epigenetic landscape of HCV-specific CD8+ T cells are required to unravel whether this molecular scar is linked to epigenetic imprinting.

The molecular scar of $T_{ML/HCV}$ cells seems to be determined by antigen recognition. In particular, we also observed a chronic signature in $T_{ML/HCV}$ cells targeting variant epitopes. Since viral escape is an early event in HCV infection typically occurring within the first 6 months[36,37] and, consequently, HCV-specific CD8+ T cells targeting variant epitopes only experience strong antigen recognition in a limited time span, these data indicate that the chronic signature in HCV-specific CD8+ T cells is already induced early during cHCV. However, the molecular scar of $T_{ML/HCV}$ cells targeting variant epitopes differed from those targeting conserved epitopes that showed a more exhausted phenotype. Thus, the dynamics of antigen recognition including duration, quantity and quality probably shape the chronic signature in exhausted virus-specific CD8+ T cells in humans. However, further studies are required to address the question of the dominant determinant, timing versus quantity and quality of antigen recognition, resulting in a 'gradual' chronic signature of HCV-specific CD8+ T cells in the context of viral escape.

The identification of an antigen-driven chronic scar within $T_{ML/HCV}$ cells that is maintained after HCV cure has several translational implications. First, it suggests a limited protective capacity of $T_{ML/HCV}$ cells in HCV reinfection. Indeed, viral relapse after HCV cure lead to a rapid recall response that, however, failed to control the infection[21]. Second, an immediate reduction or clearance of antigen is required to limit the development of a chronic scar within virus-specific CD8+ T cells. This is, for example, supported by the finding that immune restoration is possible after early but not late antiviral therapy against HCV[38]. Similarly, mouse studies have shown that early antigen removal rescues CD8+ T cells from differentiation into exhaustion[39]. Finally, our results indicate that the chronic scar of $T_{ML/HCV}$ subsets has to be targeted therapeutically in addition to antigen withdrawal to induce their full effector potential.

Online content

Any methods, additional references, Nature Research reporting summaries, source data, extended data, supplementary information, acknowledgements, peer review information; details of author contributions and competing interests; and statements of data and code availability are available at https://doi.org/10.1038/s41590-020-00817-w.

Received: 5 May 2020; Accepted: 6 October 2020;
Published online: 04 January 2021

References

1. Blank, C. U. et al. Defining 'T cell exhaustion'. *Nat. Rev. Immunol.* **19**, 665–674 (2019).
2. Gallimore, A. et al. Induction and exhaustion of lymphocytic choriomeningitis virus–specific cytotoxic T lymphocytes visualized using soluble tetrameric major histocompatibility complex class I–peptide complexes. *J. Exp. Med.* **187**, 1383–1393 (1998).
3. Moskophidis, D., Lechner, F., Pircher, H. & Zinkernagel, R. M. Virus persistence in acutely infected immunocompetent mice by exhaustion of antiviral cytotoxic effector T cells. *Nature* **362**, 758–761 (1993).
4. Zajac, A. J. et al. Viral immune evasion due to persistence of activated T cells without effector function. *J. Exp. Med.* **188**, 2205–2213 (1998).
5. Doering, T. A. et al. Network analysis reveals centrally connected genes and pathways involved in CD8$^+$ T cell exhaustion versus memory. *Immunity* **37**, 1130–1144 (2012).
6. McLane, L. M., Abdel-Hakeem, M. S. & Wherry, E. J. CD8 T cell exhaustion during chronic viral infection and cancer. *Annu. Rev. Immunol.* **37**, 457–495 (2019).
7. Wherry, E. J. & Kurachi, M. Molecular and cellular insights into T cell exhaustion. *Nat. Rev. Immunol.* **15**, 486–499 (2015).
8. Bengsch, B. et al. Deep immune profiling by mass cytometry links human T and NK cell differentiation and cytotoxic molecule expression patterns. *J. Immunol. Methods* **453**, 3–10 (2018).
9. Barili, V. et al. Targeting p53 and histone methyltransferases restores exhausted CD8$^+$ T cells in HCV infection. *Nat. Commun.* **11**, 604 (2020).
10. Fisicaro, P. et al. Targeting mitochondrial dysfunction can restore antiviral activity of exhausted HBV-specific CD8$^+$ T cells in chronic hepatitis B. *Nat. Med.* **23**, 327–336 (2017).
11. Kurktschiev, P. D. et al. Dysfunctional CD8$^+$ T cells in hepatitis B and C are characterized by a lack of antigen-specific T-bet induction. *J. Exp. Med.* **211**, 2047–2059 (2014).
12. Alfei, F. et al. TOX reinforces the phenotype and longevity of exhausted T cells in chronic viral infection. *Nature* **571**, 265–269 (2019).
13. Khan, O. et al. TOX transcriptionally and epigenetically programs CD8$^+$ T cell exhaustion. *Nature* **571**, 211–218 (2019).
14. Scott, A. C. et al. TOX is a critical regulator of tumour-specific T cell differentiation. *Nature* **571**, 270–274 (2019).
15. Yao, C. et al. Single-cell RNA-seq reveals TOX as a key regulator of CD8$^+$ T cell persistence in chronic infection. *Nat. Immunol.* **20**, 890–901 (2019).
16. He, R. et al. Follicular CXCR5-expressing CD8$^+$ T cells curtail chronic viral infection. *Nature* **537**, 412–428 (2016).
17. Im, S. J. et al. Defining CD8$^+$ T cells that provide the proliferative burst after PD-1 therapy. *Nature* **537**, 417–421 (2016).
18. Paley, M. A. et al. Progenitor and terminal subsets of CD8$^+$ T cells cooperate to contain chronic viral infection. *Science* **338**, 1220–1225 (2012).
19. Utzschneider, D. T. et al. T cell factor 1-expressing memory-like CD8$^+$ T cells sustain the immune response to chronic viral infections. *Immunity* **45**, 415–427 (2016).
20. Utzschneider, D. T. et al. T cells maintain an exhausted phenotype after antigen withdrawal and population reexpansion. *Nat. Immunol.* **14**, 603–610 (2013).
21. Wieland, D. et al. TCF1$^+$ hepatitis C virus-specific CD8$^+$ T cells are maintained after cessation of chronic antigen stimulation. *Nat. Commun.* **8**, 15050 (2017).
22. Aregay, A. et al. Elimination of hepatitis C virus has limited impact on the functional and mitochondrial impairment of HCV-specific CD8$^+$ T cell responses. *J. Hepatol.* **71**, 889–899 (2019).
23. Bengsch, B. et al. Coexpression of PD-1, 2B4, CD160 and KLRG1 on exhausted HCV-specific CD8$^+$ T cells is linked to antigen recognition and T cell differentiation. *PLoS Pathog.* **6**, e1000947 (2010).
24. Burchill, M. A., Golden-Mason, L., Wind-Rotolo, M. & Rosen, H. R. Memory re-differentiation and reduced lymphocyte activation in chronic HCV-infected patients receiving direct-acting antivirals. *J. Viral Hepat.* **22**, 983–991 (2015).
25. Cox, A. L. et al. Comprehensive analyses of CD8$^+$ T cell responses during longitudinal study of acute human hepatitis C. *Hepatology* **42**, 104–112 (2005).
26. Golden-Mason, L. et al. Upregulation of PD-1 expression on circulating and intrahepatic hepatitis C virus-specific CD8$^+$ T cells associated with reversible immune dysfunction. *J. Virol.* **81**, 9249–9258 (2007).
27. Martin, B. et al. Restoration of HCV-specific CD8$^+$ T cell function by interferon-free therapy. *J. Hepatol.* **61**, 538–543 (2014).
28. Urbani, S. et al. PD-1 expression in acute hepatitis C virus (HCV) infection is associated with HCV-specific CD8 exhaustion. *J. Virol.* **80**, 11398–11403 (2006).
29. Kim, H. D. et al. Association between expression level of PD-1 by tumor-infiltrating CD8$^+$ T cells and features of hepatocellular carcinoma. *Gastroenterology* **155**, 1936–1950 (2018).
30. Miller, B. C. et al. Subsets of exhausted CD8$^+$ T cells differentially mediate tumor control and respond to checkpoint blockade. *Nat. Immunol.* **20**, 326–336 (2019).
31. Herman, J. S., Sagar & Grun, D. FateID infers cell fate bias in multipotent progenitors from single-cell RNA-seq data. *Nat. Methods* **15**, 379–386 (2018).
32. Haghverdi, L., Buttner, M., Wolf, F. A., Buettner, F. & Theis, F. J. Diffusion pseudotime robustly reconstructs lineage branching. *Nat. Methods* **13**, 845–848 (2016).
33. Man, K. et al. Transcription factor IRF4 promotes CD8$^+$ T cell exhaustion and limits the development of memory-like T cells during chronic infection. *Immunity* **47**, 1129–1141 (2017).
34. Philip, M. et al. Chromatin states define tumour-specific T cell dysfunction and reprogramming. *Nature* **545**, 452–456 (2017).
35. Siddiqui, I. et al. Intratumoral Tcf1$^+$PD-1$^+$CD8$^+$ T cells with stem-like properties promote tumor control in response to vaccination and checkpoint blockade immunotherapy. *Immunity* **50**, 195–211 (2019).
36. Cox, A. L. et al. Cellular immune selection with hepatitis C virus persistence in humans. *J. Exp. Med.* **201**, 1741–1752 (2005).
37. Wolski, D. et al. Early transcriptional divergence marks virus-specific primary human CD8$^+$ T cells in chronic versus acute infection. *Immunity* **47**, 648–663 (2017).
38. Abdel-Hakeem, M. S. et al. Comparison of immune restoration in early versus late alpha interferon therapy against hepatitis C virus. *J. Virol.* **84**, 10429–10435 (2010).
39. Angelosanto, J. M., Blackburn, S. D., Crawford, A. & Wherry, E. J. Progressive loss of memory T cell potential and commitment to exhaustion during chronic viral infection. *J. Virol.* **86**, 8161–8170 (2012).

Methods

Study cohort. Participants were recruited at the Department of Medicine II of the University Hospital Freiburg, Germany. Thirty-two HLA-A*02-positive individuals and one HLA-B*27:05-positive individual with cHCV infection were included in this study, as well as eight HLA-A*02:01-positive individuals with acute rHCV infection (anti-HCV positive, HCV-RNA negative). Fifteen individuals chronically infected with HCV were followed through DAA therapy. All participants included in the study were infected with HCV genotype 1a or 1b. Viral loads were determined as part of the clinical diagnostics at the University Hospital Freiburg. Four-digit HLA typing was performed by next-generation sequencing run on a MiSeq system using commercially available primers (GenDx). Characteristics of the participant cohort can be found in Supplementary Table 1. Written informed consent was obtained from all participants, and the study was conducted according to federal guidelines, local ethics committee regulations (Albert-Ludwigs-Universität; 474/14; 275/15; 516/19) and the Declaration of Helsinki (1975).

Peripheral blood mononuclear cell isolation. Peripheral blood mononuclear cells (PBMCs) from EDTA-anticoagulated participant blood were isolated by density gradient centrifugation using Pancoll (Pan-Biotech). For data comparability, all PBMC samples from one participant undergoing therapy were frozen and thawed simultaneously at the day of experiment with exception of the sorting for single-cell transcriptome analysis. PBMCs were thawed in complete medium (RPMI 1640 with 10% FBS, 1% penicillin–streptomycin and 1.5% 1 M HEPES at pH 7.2–7.5 (Life Technologies and Thermo Fisher Scientific) and incubated for 15–30 min in complete medium containing 35 U ml^{-1} benzonase (Sigma-Aldrich/Merck) before processing.

Magnetic bead-based enrichment of antigen-specific CD8$^+$ T cells. For magnetic bead-based enrichment of HCV-specific CD8$^+$ T cell, PBMCs were incubated with peptide-loaded HLA tetramers coupled to phycoerythrin (PE). Subsequent enrichment was performed with anti-PE beads using magnetic-activated cell sorting (MACS) technology (Miltenyi Biotec) according to the manufacturer's protocol. Enriched HCV-specific CD8$^+$ T cells were used for multiparametric flow cytometry and transcriptome analysis. Epitope-specific HLA tetramers were generated by conjugation of biotinylated peptide-MHC class I monomers with PE-conjugated streptavidin at a HLA:strepatividin molar ratio of 5:1. The following peptide-loaded HLA tetramers were used: $NS3_{1073}$(CINGVCWTV)/HLA-A*02:01; $NS3_{1406}$(KLVALGINAV/KLSGLGLNAV)/HLA-A*02:01; and $NS5B_{2841}$(ARMILMTHF)/HLA-B*27:05.

Multiparametric flow cytometry. The following reagents and their dilutions were used for multiparametric flow cytometry: anti-Bcl-2 (100, 1:100), anti-CCR7 (G043H7, 1:50; 1:30), anti-CD127 (A019D5, 1:30; 1:100), anti-CD39 (A1, 1:30), anti-CD45RA (HI100, 1:200), anti-PD-1 (EH12.2H7, 1:30), anti-IFN-γ (4S.B3, 1:50), anti-TNF (Mab11, 1:145) (BioLegend); anti-CD8 (RPA-T8, 1:400; 1:100), anti-CD137 (4B4-1, 1:20), anti-CD45RA (HI100, 1:800), anti-PD-1 (EH12.1, 1:30), anti-IFN-γ (25723.11, 1:30), anti-TNF (MAb11, 1:50), (BD Biosciences); anti-CD14 (61D3; 1:100), anti-CD19 (HIB19, 1:100), anti-CD38 (HB7, 1:200), anti-IRF4 (3E4, 1:50), anti-TOX1 (TRX10, 1:100), anti-EOMES (WD1928; 1:50), anti-T-bet (4B10, 1:200) (eBioscience); and anti-TCF-1 (C63D9, 1:100) (Cell Signaling). A fixable viability dye (eFluor 780, 1:200; eBioscience) was used for live/dead discrimination. Staining of intranuclear or cytoplasmic molecules was performed with the FOXP3/Transcription Factor Staining Buffer Set (eBioscience). Cells were fixed with 2% paraformaldehyde before acquisition on an LSRFortessa (BD Biosciences). Machine and measurement standardization were performed by applying the Cytometer Setup & Tracking beads (BD Biosciences) to optimize and standardize cytometer setup. Analysis of the data was performed using FlowJo version 10.6.2 (Treestar and Becton Dickinson). To ensure that the analyzed, virus-specific CD8$^+$ T cells actually encountered antigen, CD45RA$^+$CCR7$^+$ naive virus-specific CD8$^+$ T cells were excluded, as well as dead cells. In addition, we did not further analyze cell (sub)populations consisting of less than five cells. For manual gating, data are depicted as frequencies, cell counts (per ml; based on whole-blood cell count obtained in the clinical diagnostics) or median fluorescence intensity (MFI) normalized to the MFI of the respective naive CD8$^+$ T cells.

Dimensionality reduction of multiparameter flow cytometry data. The visualization of multiparametric flow cytometry data was performed using CyTOF workflow R package version 1.12.0 (ref. [40]). The analysis was performed on two separate panels: panel 1 (surface markers) contained CD127, PD-1, CD38, CD39, CD137 and CCR7; and panel 2 (transcription factors) comprised TOX, TCF-1, Bcl-2, CCR7, CD127, PD-1, IRF4, T-bet and EOMES. Marker intensities were transformed using arcsinh (inverse hyperbolic sine) with a cofactor of 150. The dimensionality reduction on the transformed data was performed using *t*-SNE, except for flow cytometry data presented in Fig. 3. Diffusion maps were used for dimensionality reduction of the dataset shown in Fig. 3. To facilitate the visualization of different samples, cells were downsampled to match the sample with the lowest number of cells before dimensionality reduction.

Cytokine production. Cytokine production of virus-specific CD8$^+$ T cells was assessed after 14 d of in vitro expansion and restimulation of the cells with epitope-specific peptides in the presence of brefeldin A (GolgiPlug; 0.5 µl ml^{-1}) and monensin (GolgiStop; 0.325 µl ml^{-1}) (BD Biosciences) for 5 h at 37 °C. Stimulation with phorbol 12-myristate 13-acetate (50 ng ml^{-1}; Sigma) and ionomycin (1 µg ml^{-1}; Sigma) served as positive control. In vitro expansion was performed with $1–2 \times 10^6$ PBMCs, stimulated with epitope-specific peptides (10 µg ml^{-1}), anti-CD28 (clone CD28.2, 0.5 µg ml^{-1}) (BD Biosciences) and medium supplemented with rIL-2 (Miltenyi Biotec).

Viral sequencing. RNA was extracted from participants' sera using the QIAmp viral RNA minikit (Qiagen). Reverse transcription was performed according to the manufacturer's instructions (RT; SuperScript III First-Strand Kit, Invitrogen) followed by DNA amplification via nested PCR (GoTaq G2 Flexi DNA Polymerase Kit, Promega) following the manufacturer's protocols. The following specific primers were used: HCV genotype 1a: 5735R (5′-GAGGACCTTCCCCAGYCC-3′), 2549F (5′-CGTCTGCTCCTGCTTGTGG-3′), 4905R (5′AGCACAGCCYGCGTC ATAGC-3′), 2740F (5’-ATGTGGCCTCTCCTCCTGC-3′), 9331R (5′-GCAGCRA GCAGGAGTAGGC-3′), 7282F (5′-AACCACCTGTGGTCCATGG-3′), 9155R (5′-TTGCCACATATGGCAGCC-3′), 7603F (5′-GGARGAYGTCGTGTGC TGC-3′); HCV genotype 1b: 5534R (5′-TCTGCTTGAAYTGCTCGGC-3′), 2954F (5′-GCCGCGATGCCATCATCC-3′), 4978R (5′-GGTGTATTTAGGTAAGCCC GC-3′), 3249F (5′-TTGCGGTGGCAGTHGAGC-3′), 8537R (5′-CTTYGCAGCT CGACAGGC-3′), 6833F (5′-TCACAGCTCCCATGYGAGCC-3′), 8143R (5′-TAR AGGGCCATYTTCTCGC-3′), 9308R (5′-GCTGTGATAWATGTCTCCCCCG-3′), 8274F (5′-TATGAYACCCGCTGYTTYGACTC-3′). Sanger sequencing was performed at Eurofins Genomics.

Low-input RNA sequencing. HCV-specific CD8$^+$ T cells were enriched by magnetic bead-based enrichment, and surface staining was performed. Live HCV-specific CD8$^+$ T cell populations were sorted with a FACSMelody Cell Sorter (Becton Dickinson). Naive, CD45RA$^+$CCR7$^+$ T cells were excluded and different subpopulations of virus-specific CD8$^+$ T cells sorted based on CD127 and PD-1 coexpression (Fig. 1 and Extended Data Fig. 1). Roughly 100 cells were sorted into 1× reaction buffer and prepared for low-input transcriptome analysis with SMART-Seq v4 Ultra Low-input RNA Kit (Clontech Laboratories). Sequencing was performed at the EMBL Genomics Core Facility (Heidelberg) using an Illumina NextSeq 500 platform with 75-bp paired-ends reads.

Low-input RNA sequencing data alignment. Sequenced RNA reads were aligned to the human reference genome (build 37, version hs37d5 from the 1000 Genome Project Phase 3). The mapping tool STAR (version 2.5.2b)[41] was used, employing a two-pass alignment. The parameters used were: --sjdbOverhang 200 --runThreadN 8 --outSAMtype BAM Unsorted SortedByCoordinate --limitBAMsortRAM 100000000000 --outBAMsortingThreadN=1 --outSAMstrandField intronMotif --outSAMunmapped Within KeepPairs --outFilterMultimapNmax 1 --outFilterMismatchNmax 5 --outFilterMismatchNoverLmax 0.3 --twopassMode Basic --twopass1readsN -1 --genomeLoad NoSharedMemory --chimSegmentMin 15 --chimScoreMin 1 --chimScoreJunctionNonGTAG 0 --chimJunctionOverhangMin 15 --chimSegmentReadGapMax 3 --alignSJstitchMismatchNmax 5 -1 5 5 --alignIntronMax 1100000 --alignMatesGapMax 1100000 --alignSJDBoverhangMin 3 --alignIntronMin 20 --clip3pAdapterSeq CTGTCTCTTATACACATCT --readFilesCommand gunzip -c. All other parameters were set to default. Reads were position sorted using SAMtools (version 1.6)[42]. Duplicate read marking was performed using sambamba (version 0.6.5)[43] with eight threads. BAM file indexes were generated using sambamba. Quality control was performed using the rnaseqc tool (version v1.1.8.1)[44] with the 1000 Genomes assembly and gencode 19 gene models and no depth of coverage analysis, and also using samtools flagstat. An extensive list of quality-control statistics for each sample is available in Supplementary Table 2. For gene strand unspecific read counting was perfomed over exons of the gencode v19 gene models using featureCounts v1.5.1, counting only uniquely mapping reads indicated by a mapping quality of 255 by STAR. For calculation of total library abundance (for FPKM/TPM calculations), every gene on chromosomes X and Y, MT and ribosomal RNA and transfer RNA were omitted to avoid library size estimation biases that they may introduce.

Differential gene expression, enrichment and network analysis of low-input RNA sequencing data. Bioinformatic analyses were performed using common protocols with the references listed. Differential expression analysis was performed by the DESeq2 package[45] (Supplementary Table 3). GSEA was performed using the fgsea package by taking the log2 FC value to rank genes. GO and KEGG enrichment on significant DEGs were performed using clusterProfiler[46] (Supplementary Table 3). Coexpression network analysis was performed by the WGCNA package[47]. Consensus clustering was performed using the cola package. The ATC method was used to select feature genes and spherical *k*-means clustering was applied to partition samples. Genes that were significantly different between sample groups were selected by one-way ANOVA (false discovery rate < 0.05).

TCR clonotype analysis of low-input RNA sequencing data. MiXCR version 2.1.12 (ref. [48]) was used to identify CDR3 clonotypes from the individual FASTQ files of the RNA-seq samples using the align and assemble commands with default options. These clonotypes were further analyzed using Vdjtools version 1.19 for post hoc analysis of TCR repertoires, using Java version 1.8.0_40 and R version 3.3.1. The MiXCR metadata file was initially converted, and basic statistics and segment usage was evaluated using the CalcBasicStats and CalcSegmentUsage commands. After manual quality assurance, clonotype quantile statistics were calculated using the PlotQuantileStats command, which produced the three-layer donut charts visualizing the repertoire clonality: the first (inner) layer of the donut chart showed singleton, doubleton and higher-order clonotypes; the second layer of the donut chart displayed the top percentiles of clonotypes from the higher-order clonotypes; and the third (outer) layer displayed individual abundances of most recurrent clonotypes.

Single-cell sorting. Single non-naive HCV-specific CD8$^+$ T cells were sorted in 384-well plates (Bio-Rad) containing lysis buffer and mineral oil using FACSMelody Cell Sorter (Becton Dickinson). The sorter was run on single-cell sort mode. Using pulse geometry gates (FSC-W × FSC-H and SSC-W × SSC-H), doublets were excluded. After the completion of sorting, the plates were centrifuged for 10 min at 2,200*g* at 4°C, snap frozen in liquid nitrogen and stored at −80°C until processed.

Single-cell RNA amplification and library preparation. scRNA-seq was performed using the mCEL-Seq2 protocol, an automated and miniaturized version of CEL-Seq2 on a mosquito nanoliter-scale liquid-handling robot (TTP LabTech)[31,49]. Twenty-two libraries with 96 cells each were sequenced per lane on an Illumina HiSeq 3000 sequencing system (pair-end multiplexing run) at a depth of ~130,000–200,000 reads per cell. Sequencing was performed at the sequencing facility of the Max Planck Institute of Immunobiology and Epigenetics.

Single-cell sequencing data alignment and quantification of transcript abundance. Paired-end reads were aligned to the transcriptome using bwa (version 0.6.2-r126) with default parameters[50]. The transcriptome contained all gene models based on the human whole-genome ENCODE V24 release. All isoforms of the same gene were merged to a single gene locus. Furthermore, gene loci overlapping by >75% were merged to larger gene groups. The right mate of each read pair was mapped to the ensemble of all gene loci and to the set of 92 External RNA Control Consortium spike-ins in sense direction[51]. Reads mapping to multiple loci were discarded. The left read contains the barcode information: the first six bases corresponded to the unique molecular identifier (UMI) followed by six bases representing the cell-specific barcode. The remainder of the left read contains a polyT stretch. For each cell barcode, the number of UMIs per transcript was counted and aggregated across all transcripts derived from the same gene locus. Based on binomial statistics, the number of observed UMIs was converted into transcript counts[52].

Bioinformatic analysis of single-cell RNA sequencing data. Clustering analysis and visualization were performed using the RaceID3 algorithm[31]. Approximately 26,214 and 18,665 genes were quantified in the cHCV and cured HCV datasets, respectively. In the combined analysis of individuals with cHCV and cured individuals, 27,336 genes were detected. Few contaminating B cells based on the expression of marker genes such as *CD79A*, *IGLC2*, *IGLC3* and *IGKC* were excluded from the analysis. For the analysis of cHCV, cured HCV and the combined dataset, cells with a total number of transcripts < 800 were discarded, and count data of the remaining cells were normalized by downscaling. Cells expressing >2% of *KCNQ1OT1*, a potential marker for low-quality cells[53], were not considered for analysis. Additionally, transcripts correlating to *KCNQ1OT1* with a Pearson's correlation coefficient > 0.4 were removed. We observed heterogeneity between participants in the dataset, which was corrected using the mnnCorrect function from the scran package implemented in the RaceID3 (ref. [54]). The following parameters were used for RaceID3 analysis: mintotal = 800, minexpr = 3, minnumber = 3, probthr = 0.0001, knn = 10 and bmode = scran. Cells from each participant were considered a batch. Dimensionality reduction for visualization was performed using the compfr function of RaceID3, which provides a *k*-nearest neighbor graph layout utilizing the Fruchterman–Rheingold algorithm. The number of nearest neighbors was set to 10.

DPT analysis on the cHCV dataset was performed using the destiny R package[32]. The genes included in the DPT analysis were obtained using the getfdata function of RaceID3. The number of nearest neighbors *k* was set to 10. SOMs were generated using the FateID package on the basis of the ordering computed by DPT as input. Only genes with >2 counts after size normalization in at least three cells were included in the SOM analysis. In brief, smooth zonation profiles were derived by applying local regression on normalized transcript counts after ordering cells by DPT. Next, a one-dimensional SOM with 1,000 nodes was computed on these profiles after *z*-transformation. Neighboring nodes were merged if the Pearson's correlation coefficient of the average profiles of these nodes exceeded 0.85. Nodes of the SOM with less than five transcripts were discarded.

Differential gene expression analysis was performed using the diffexpnb function of RaceID3 algorithm. DEGs between two subgroups of cells were identified similar to a previously published method[55] (Supplementary Table 3). First, negative binomial distributions reflecting the gene expression variability within each subgroup were inferred based on the background model for the expected transcript count variability computed by RaceID3. Using these distributions, a *P* value for the observed difference in transcript counts between the two subgroups was calculated and multiple testing corrected by the Benjamini–Hochberg method.

Using the quadratic-programming approach to quantify cell similarities between individuals with cHCV and cured individuals, we calculated weights for all cluster medoids in the cured HCV dataset for each cell in the cHCV dataset using the solve.QP function of the quadprog R package. For example, to calculate the weights for all cluster medoids of the cured HCV data for each cell in the cHCV data, the cHCV normalized transcript count matrix containing genes as rows and single cells as columns and the cured HCV normalized transcript count matrix containing genes as rows and cluster medoids as columns were provided as inputs to the Dmat and dvec arguments of the solve.QP function, respectively. Cluster medoids were calculated by the compmedoids function of the RaceID3 algorithm. The intersect of feature genes expressed in both datasets was used for calculating the weights using quadratic programming.

Statistics. Statistical analysis of flow cytometric data and investigation of cell counts, viral loads and TCR clonotypes was performed with GraphPad 8 (Prism). Kruskal–Wallis test (one-sided) including Dunn's multiple-comparison test was used (Figs. 1b–d, 3e, 5c,f,g and Extended Data Figs. 2f, 3b, 4b, 5b, 7a, 8b and 9b), as well as Mann–Whitney comparison test (two-sided; Fig. 2d and Extended Data Figs. 2d, 4c and 6a) and Wilcoxon matched-pairs signed-rank test (two-sided; Extended Data Fig 4c). GSEA was performed using the fgsea package by taking the log2 FC value to rank genes (one-sided; Figs. 2a–c, 4c and 6e). DEG analysis (two-sided) of the low-input RNA-seq data was performed using the R package fgsea (Figs. 4d and 6d and Extended Data Fig. 2a). GO and KEGG enrichment on the significant DEGs were performed by the clusterProfiler package (one-sided; Figs. 4e and 6d). The statistical analysis of the aggregated transcript counts and normalized expression values of scRNA-seq data was analyzed by Wilcoxon matched-pairs signed-rank test (two-sided; Figs. 3d,e and 5b and Extended Data Fig. 3a). Differential gene expression analysis was performed using the diffexpnb function of RaceID3 algorithm (Fig. 5d). Further information on the statistics of low-input and scRNA-seq analysis can be found in the corresponding method sections. Exact *P* values are indicated in the figures.

Reporting Summary. Further information on research design is available in the Nature Research Reporting Summary linked to this article.

Data availability

The primary read files and expression count files for the scRNA-seq datasets reported in this paper are available to download from the Gene Expression Omnibus (GEO) under accession number GSE150305. The expression count files for the low-input RNA sequencing are available to download from GEO under accession number GSE150345. The raw data files for the low-input RNA sequencing are available from the European Genome-phenome Archive under accession number EGAD00001006259. The gene sets used for GSEA were: (1) exhaustion (chronic TCF-1$^-$), memory-like (chronic TCF-1$^+$) and memory signature (https://doi.org/10.1016/j.immuni.2016.07.021)[19]; (2) PD-1^{int} CD8$^+$ TILs signature (https://doi.org/10.1053/j.gastro.2018.08.030)[29] and the TCF-1$^+$ CD8$^+$ TILs signature (https://doi.org/10.1016/j.immuni.2018.12.021)[35]. The remaining data supporting the findings of this study are available from the corresponding authors upon request.

References

40. Nowicka, M. et al. CyTOF workflow: differential discovery in high-throughput high-dimensional cytometry datasets. *F1000Res* **6**, 748 (2017).
41. Dobin, A. et al. STAR: ultrafast universal RNA-seq aligner. *Bioinformatics* **29**, 15–21 (2013).
42. Li, H. et al. The Sequence Alignment/Map format and SAMtools. *Bioinformatics* **25**, 2078–2079 (2009).
43. Tarasov, A., Vilella, A. J., Cuppen, E., Nijman, I. J. & Prins, P. Sambamba: fast processing of NGS alignment formats. *Bioinformatics* **31**, 2032–2034 (2015).
44. DeLuca, D. S. et al. RNA-SeQC: RNA-seq metrics for quality control and process optimization. *Bioinformatics* **28**, 1530–1532 (2012).
45. Love, M. I., Huber, W. & Anders, S. Moderated estimation of fold change and dispersion for RNA-seq data with DESeq2. *Genome Biol.* **15**, 550 (2014).
46. Yu, G., Wang, L. G., Han, Y. & He, Q. Y. clusterProfiler: an R package for comparing biological themes among gene clusters. *OMICS* **16**, 284–287 (2012).
47. Langfelder, P. & Horvath, S. Fast R functions for robust correlations and hierarchical clustering. *J. Stat. Softw.* **46**, i11 (2012).
48. Bolotin, D. A. et al. MiXCR: software for comprehensive adaptive immunity profiling. *Nat. Methods* **12**, 380–381 (2015).
49. Hashimshony, T. et al. CEL-Seq2: sensitive highly-multiplexed single-cell RNA-seq. *Genome Biol.* **17**, 77 (2016).

50. Li, H. & Durbin, R. Fast and accurate long-read alignment with Burrows–Wheeler transform. *Bioinformatics* **26**, 589–595 (2010).
51. Baker, S. C. et al. The external RNA controls consortium: a progress report. *Nat. Methods* **2**, 731–734 (2005).
52. Grun, D., Kester, L. & van Oudenaarden, A. Validation of noise models for single-cell transcriptomics. *Nat. Methods* **11**, 637–640 (2014).
53. Grun, D. et al. De novo prediction of stem cell identity using single-cell transcriptome data. *Cell Stem Cell* **19**, 266–277 (2016).
54. Haghverdi, L., Lun, A. T. L., Morgan, M. D. & Marioni, J. C. Batch effects in single-cell RNA-sequencing data are corrected by matching mutual nearest neighbors. *Nat. Biotechnol.* **36**, 421–427 (2018).
55. Anders, S. & Huber, W. Differential expression analysis for sequence count data. *Genome Biol.* **11**, R106 (2010).

Acknowledgements

We thank all participants in the current study and H. Pircher, I. Schulien, K. Heim, V. Oberhardt and T. Gross for critical reading of the manuscript. The work presented here was supported by the CRC/TRR 179-Project (no. 01 to R.T., no. 02 to C.N.-H., no. 04 to T.B., no. 09 to R.B., no. 20 to M.H., no. 21 to B.B. and no. Z2 to R.E. of the German Research Foundation (DFG; TRR179 project no. 272983813). M.H. was supported by a Margarete von Wrangell fellowship. D.G. was supported by the Max Planck Society, the Behrens-Weise-Foundation and the DFG (no. GR4980/3-1). D.A.P. was supported by a Wellcome Trust Senior Investigator Award (no. 100326/Z/12/Z).

Author contributions

N.H. performed and analyzed experiments with the help of D.W., K.J., J.K. and O.S. S.L.-L., E.G. and D.A.P. provided pMHC-I tetramers. F.E. performed four-digit HLA typing by next-generation sequencing. Z.G. and N.I. analyzed and interpreted low-input RNA-seq data. C.C., R.E., B.B., T.B., C.N.-H. and R.B. contributed to data interpretation. Sagar and D.G. performed scRNA-seq and analyzed the respective data. M.H. and R.T. designed the study, contributed to experimental design and planning, interpreted data and wrote the manuscript.

Competing interests

The authors declare no competing interests.

Additional information

Extended data is available for this paper at https://doi.org/10.1038/s41590-020-00817-w.

Supplementary information is available for this paper at https://doi.org/10.1038/s41590-020-00817-w.

Correspondence and requests for materials should be addressed to R.T. or M.H.

Peer review information Peer reviewer reports are available. L. A. Dempsey was the primary editor on this article and managed its editorial process and peer review in collaboration with the rest of the editorial team.

Reprints and permissions information is available at www.nature.com/reprints.

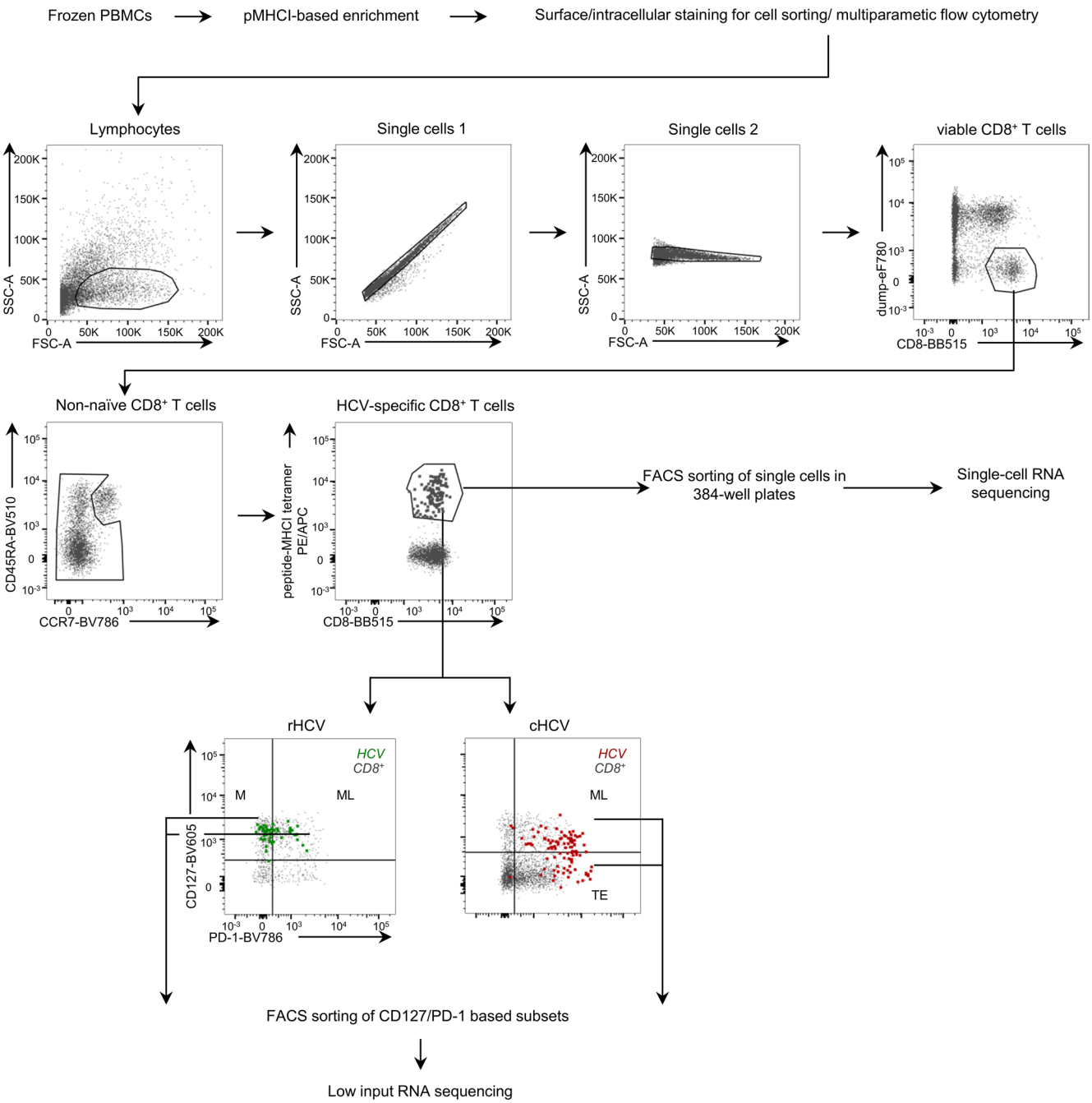

Extended Data Fig. 1 | Experimental setup. Gating strategy of flow cytometric-based analyses and sorting of HCV-specific CD8⁺ T cells for transcriptome analyses using low-input or single-cell RNAseq. Dead cells, CD14⁺ (monocytes) and CD19⁺ (B cells) cells were excluded. Naïve CD8⁺ T cells (CD45RA⁺CCR7⁺) were also excluded. HLA-A*02:01- and HLA-B*27:05-restricted HCV-specific CD8⁺ T cells were identified by peptide/MHCI tetramers and further analyzed.

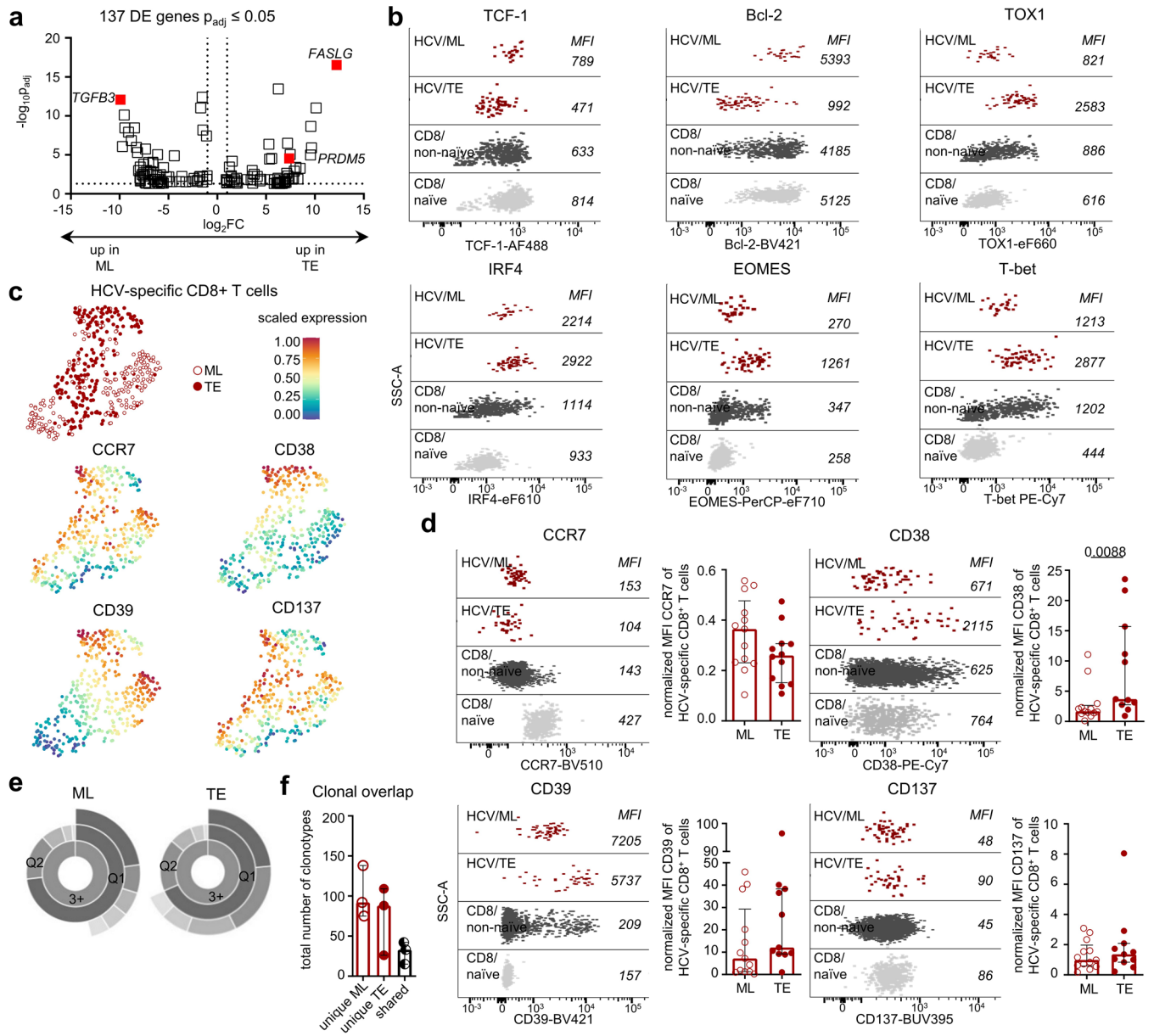

Extended Data Fig. 2 | $T_{ML/HCV}$ and $T_{TE/HCV}$ cells exhibit distinct characteristics. a, Volcano plot showing DEGs comparing low-input transcriptome data of $T_{ML/HCV}$ and $T_{TE/HCV}$ subsets (targeting conserved epitopes) derived from 3 cHCV-infected patients (red: exemplary DEGs are specified). *x*-axis represents the log_2FC; *y*-axis represents the $-log_{10}$ adjusted p values (≤ 0.05). Dotted lines indicate filter criteria of log_2FC of ± 1 and adj. p value of 0.05. **b–d**, Flow cytometric analysis including various T-cell memory and exhaustion/effector markers of $T_{ML/HCV}$ and $T_{TE/HCV}$ subsets derived from 12 cHCV patients. Representative dot plots including control analyses of non-naïve and naïve bulk $CD8^+$ T cells (**b**,**d**), t-SNE representation (**c**) and bar charts (**d**, median fluorescence intensity (MFI) normalized to naïve CD8 + T cells) are depicted. **e**,**f**, Representative overview of the TCR clonotype distribution (low-input transcriptome data) within $T_{ML/HCV}$ and $T_{TE/HCV}$ subsets from one (out of 3) cHCV patient depicted in three-layer donut plots: the inner layer depicts singleton, doubleton and high-order clonotypes; the second layer displays the top percentiles of clonotypes from the higher-order clonotypes and outer layer displays individual abundances of most recurrent clonotypes (**e**). Clonal overlap was assessed (**f**; n = 3). Bar charts show the median with IQR. Significance was assessed by Mann-Whitney comparison tests (two-sided) for flow cytometric analysis and by Kruskal-Wallis test (one-sided) including Dunn's multiple comparisons test for TCR clonotypes analysis. DEG analysis of the volcano plot (two-sided) was done by DESeq2. All p values are corrected by the Benjamini-Hochberg method.

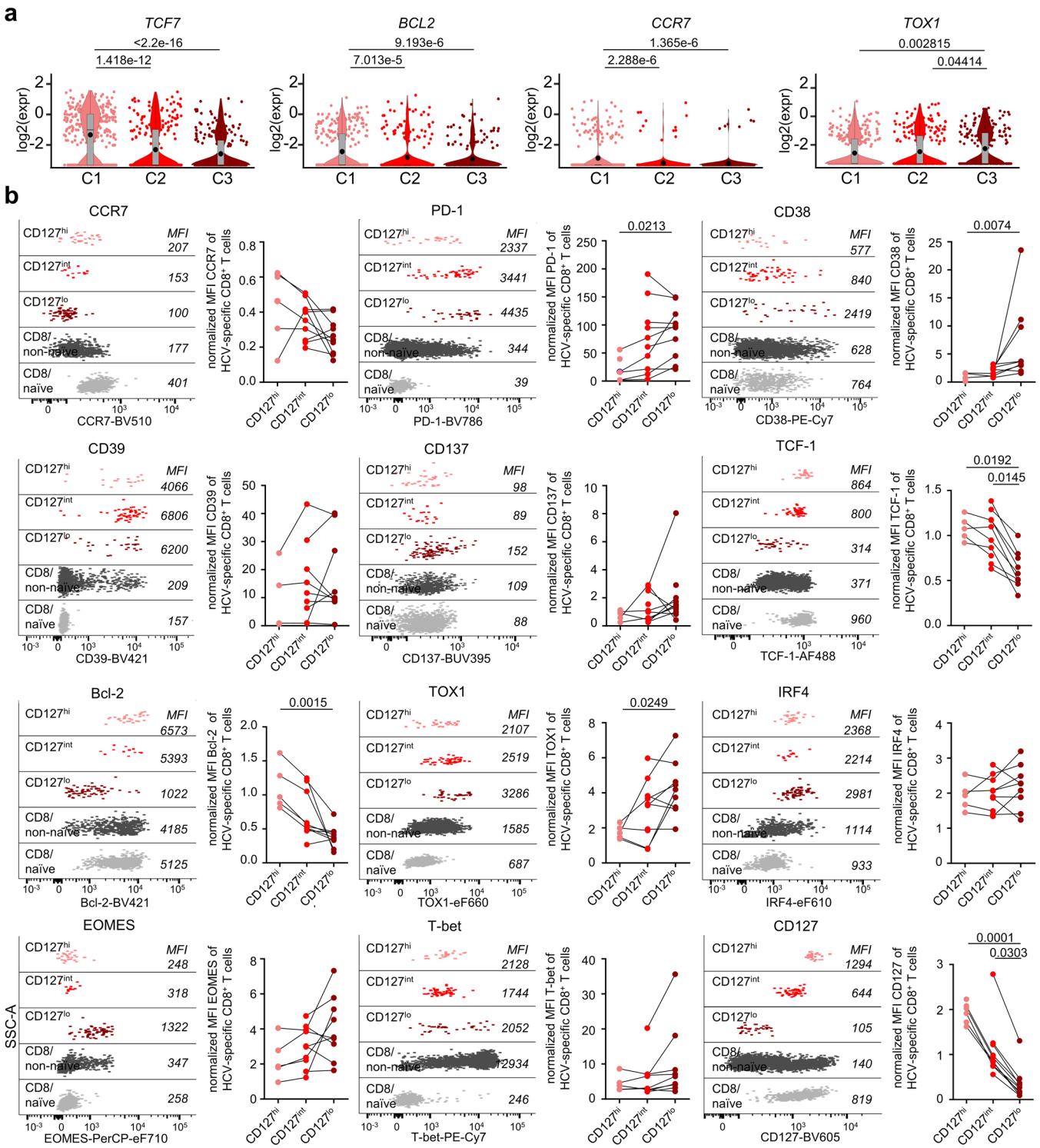

Extended Data Fig. 3 | Characterization of HCV-specific CD127^{lo}, CD127^{int} and CD127^{hi} subsets. a, mRNA expression level of *TCF7*, *BCL2*, *CCR7* and *TOX* (single-cell RNA sequencing data; n = 784 cells from 6 cHCV) in cluster 1–3 are depicted by violin plots. **b**, Flow cytometric analysis including various T cell memory and exhaustion/effector markers of CD127^{lo}, CD127^{int} and CD127^{hi} (representing cluster 1–3) HCV-specific CD8$^+$ T cells derived from 12 cHCV-infected patients. Representative dot plots are depicted including control analyses of non-naïve and naïve bulk CD8$^+$ T cells. Summary graphs display the median fluorescence intensity (MFI) of marker expression of HCV-specific CD8$^+$ T cell subsets normalized to naïve CD8$^+$ T cells. Significance was assessed by Kruskal-Wallis test (one-sided) including Dunn's multiple comparisons test for flow cytometric analysis and Wilcoxon matched-pairs signed rank test (two-sided) for mRNA expression levels. The violin plots show the frequency with box plots depicting the median with IQR.

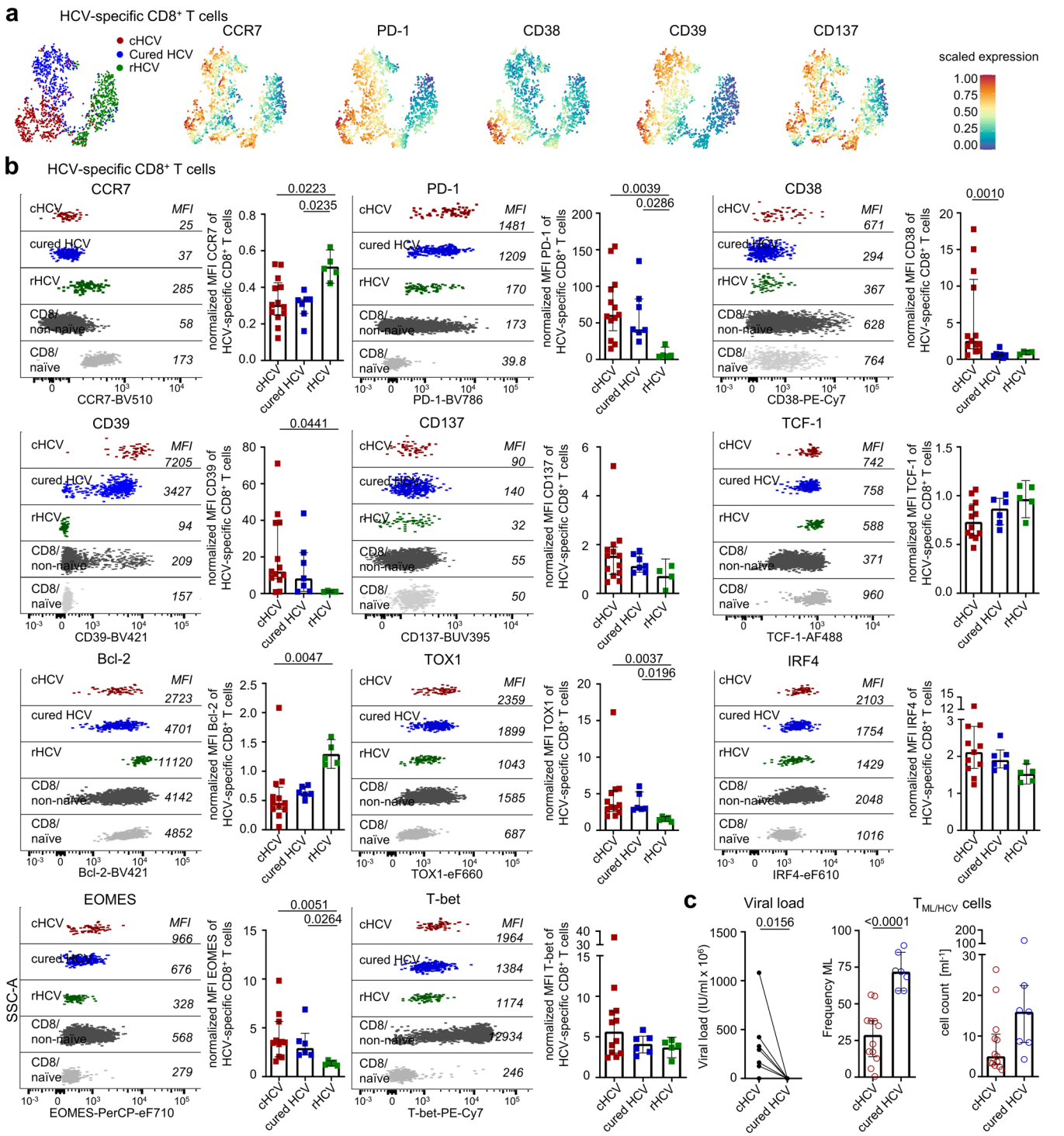

Extended Data Fig. 4 | Phenotypic characteristics of HCV-specific CD8⁺ T cells after HCV cure. Flow cytometric analysis including various T cell memory and exhaustion/effector markers of HCV-specific CD8⁺ T cells before (n = 12) and after (n = 7) HCV cure and in rHCV (n = 5). **a**, t-SNE representation with scaled expression (color code: red: high; blue: low) is depicted. **b**, Representative dot plots (including control analyses of non-naïve and naïve bulk CD8⁺ T cells) and bar charts summarizing manually gated flow cytometric data (median fluorescence intensity (MFI) normalized to naïve CD8⁺ T cells) are depicted. **c**, Serum viral loads (HCV RNA), the frequency and cell counts [/ml] of $T_{ML/HCV}$ subsets from patients before (n = 12) and after HCV cure (n = 7). Bar charts show the median with IQR. Significance was assessed by Kruskal-Wallis test (one-sided) including Dunn's multiple comparisons test (b), Mann-Whitney comparison test (two-sided) (c; right) and Wilcoxon matched-pairs signed rank test (two-sided) (c, left).

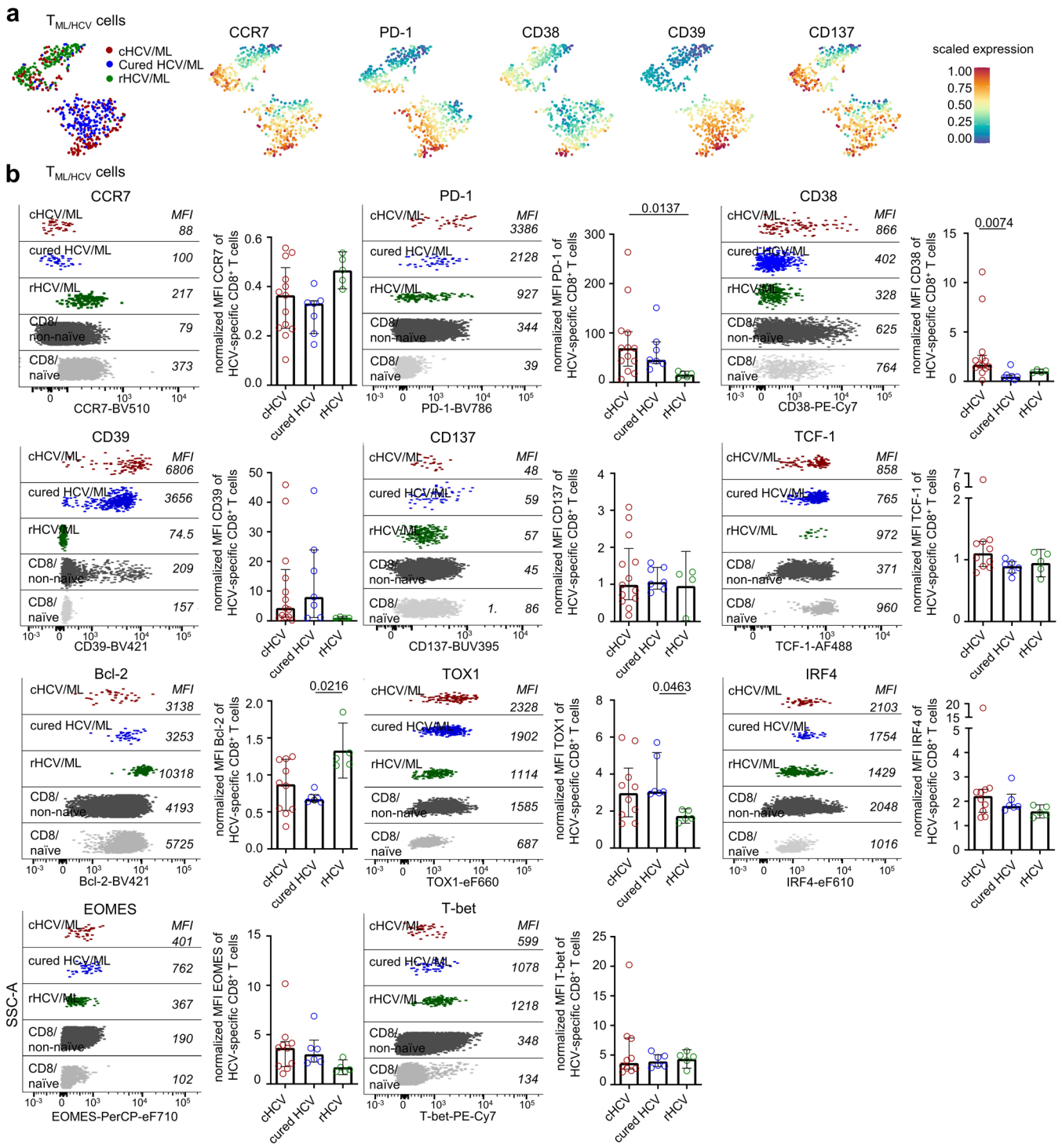

Extended Data Fig. 5 | Phenotypic characteristics of the $T_{ML/HCV}$ subset. Flow cytometric analysis including various T cell memory and exhaustion/effector markers of $T_{ML/HCV}$ cells before (n = 12) and after (n = 7) HCV cure and in rHCV (n = 5). t-SNE representation with scaled expression depicted as color code (red: high; blue: low) **a**, representative dot plots (including control analyses of non-naïve and naïve bulk $CD8^+$ T cells) and bar charts summarizing manually gated flow cytometric data (**b**; median fluorescence intensity (MFI) normalized to naïve $CD8^+$ T cells) are depicted. Bar charts show the median with IQR. Significance was assessed by Kruskal-Wallis test (one-sided) including Dunn's multiple comparisons test.

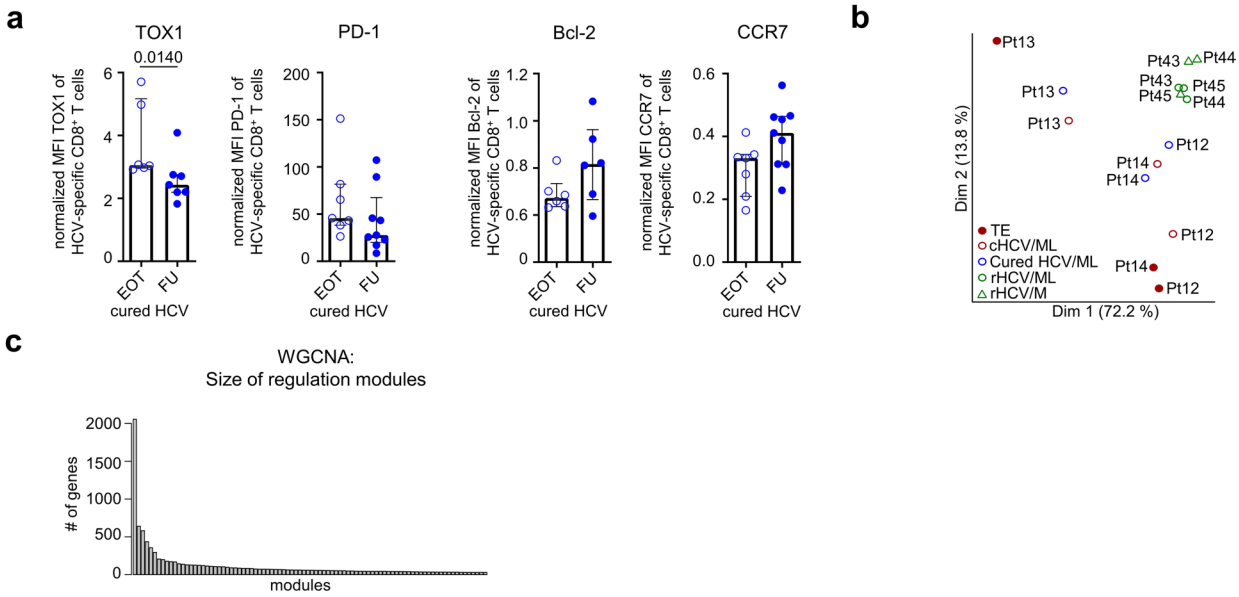

Extended Data Fig. 6 | Characteristics of $T_{ML/HCV}$ cells after HCV cure. a, Flow cytometric analysis of TOX1, PD-1, Bcl-2 and CCR7 in $T_{ML/HCV}$ subsets at the end of DAA therapy (EOT) (n = 6) and at long-term (>6 months) follow-up (FU) after HCV cure (n = 7) is depicted as bar chart (median fluorescence intensity (MFI) normalized to naïve $CD8^+$ T cells). **b**, Principle component analysis (PCA) of the transcriptomes of $T_{ML/HCV}$ subsets before and after HCV cure and in rHCV; and of $T_{TE/HCV}$ cells (cHCV) and T_M cells (rHCV) (cHCV, cured HCV, rHCV: n = 3 each). (**c**) WGCNA of low input transcriptome data was performed. Numbers of genes in each defined module are depicted in the bar chart. Bar charts show the median with IQR. Significance was assessed by Mann-Whitney comparison test (two-sided).

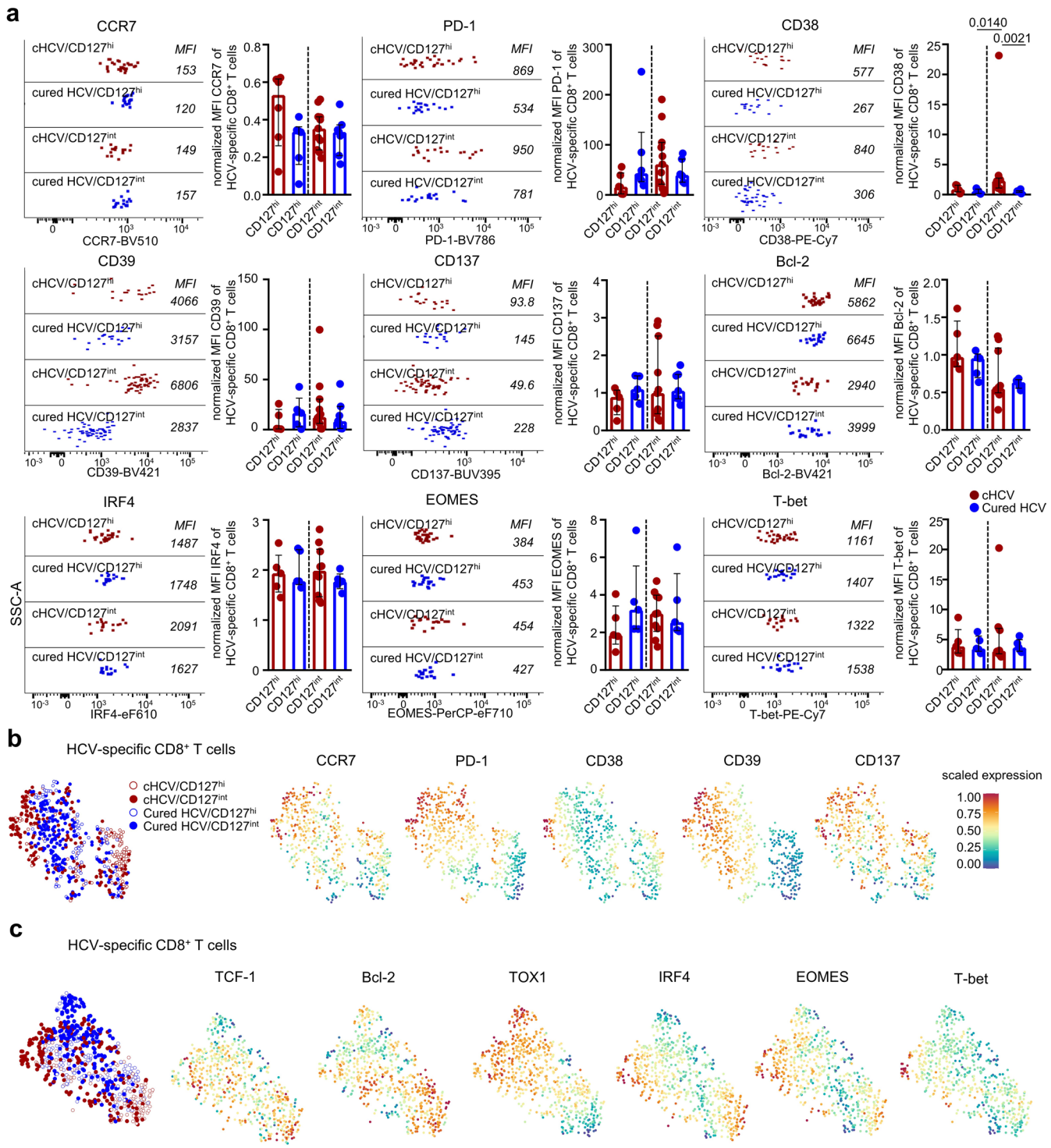

Extended Data Fig. 7 | Phenotypic characteristics of CD127^{hi} and CD127^{int} subsets before and after HCV cure. Flow cytometric analysis including various T cell memory and exhaustion/effector markers of CD127^{int} and CD127^{hi} (representing cluster 1 and 2) HCV-specific CD8 + T cells from patients before (n = 12) and after (n = 7) HCV cure. Representative dot plots (including control analyses of non-naïve and naïve bulk CD8^{+} T cells), bar charts (**a**; median fluorescence intensity (MFI) normalized to naïve CD8^{+} T cells) and t-SNE representation **b**,**c**, are depicted. Scaled expression is depicted as color code (red: high; blue: low). Bar charts show the median with IQR. Significance was assessed by Kruskal-Wallis test (one-sided) including Dunn's multiple comparisons test.

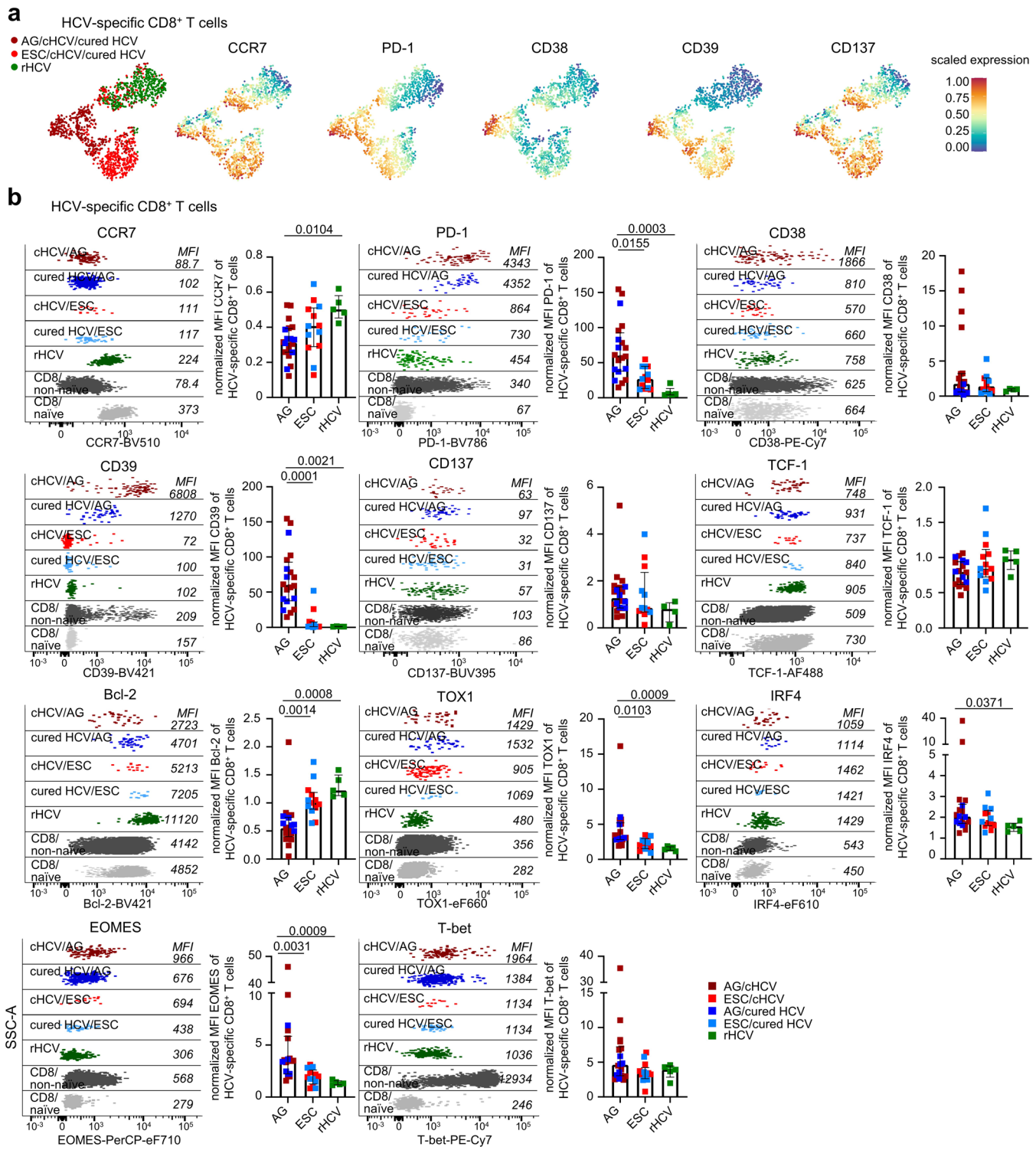

Extended Data Fig. 8 | Phenotypic characteristics of HCV-specific CD8⁺ T cells targeting conserved versus variant epitopes. Flow cytometric analysis including various T cell memory and exhaustion/effector markers of HCV-specific CD8⁺ T cells in rHCV (n = 5), cHCV and cured HCV targeting either conserved epitopes (AG; cHCV: n = 12, cured HCV: n = 7) or variant epitopes (ESC; cHCV: n = 8, cured HCV: n = 6). t-SNE representation with scaled expression depicted as color code (red: high; blue: low) **a**, representative dot plots (including control analyses of non-naïve and naïve bulk CD8⁺ T cells) and bar charts summarizing manually gated flow cytometric data (**b**; median fluorescence intensity (MFI) normalized to naïve CD8⁺ T cells) are depicted. Bar charts show the median with IQR. Significance was assessed by Kruskal-Wallis test (one-sided).

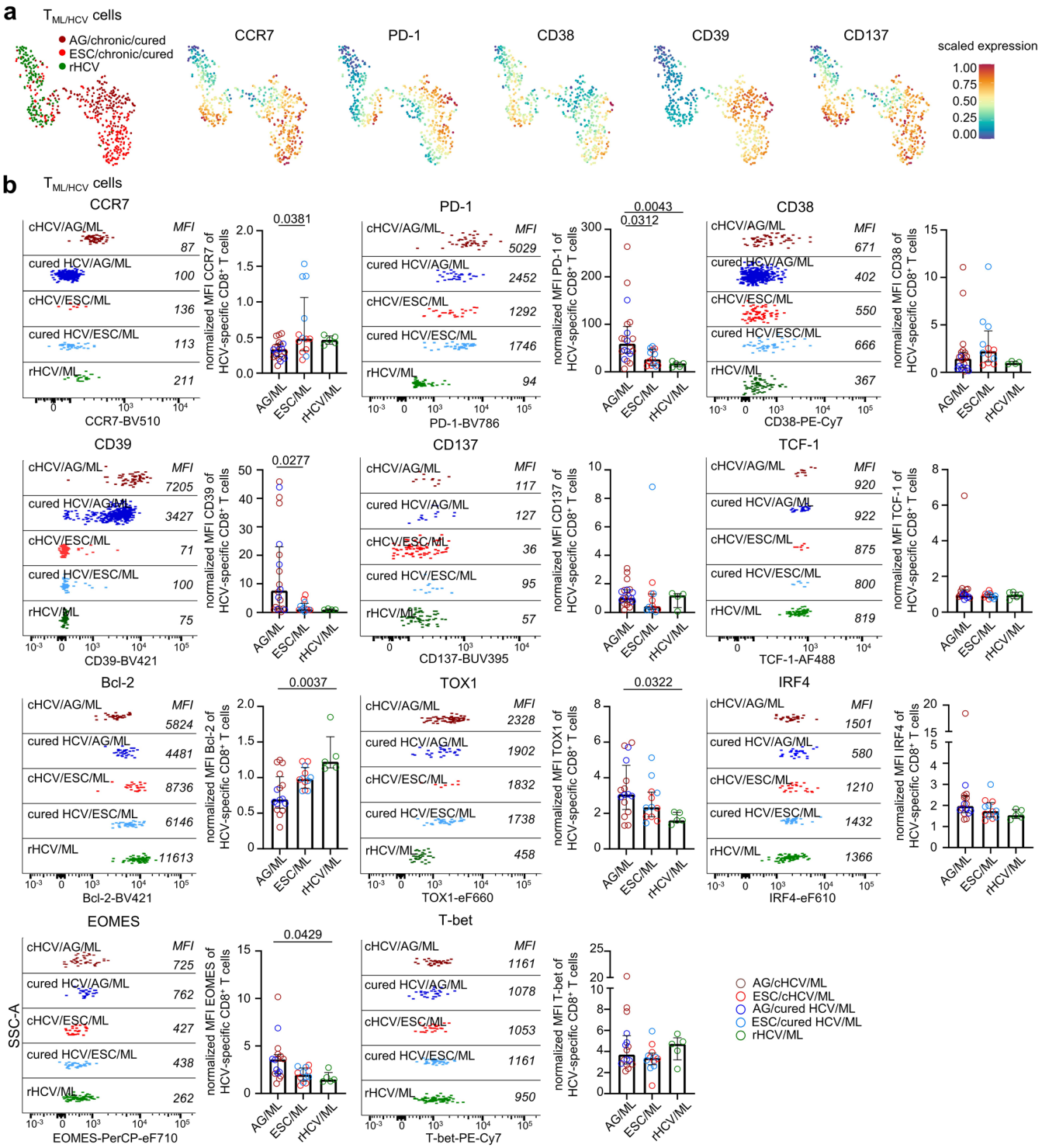

Extended Data Fig. 9 | Phenotypic characteristics of $T_{ML/HCV}$ cells targeting conserved versus variant epitopes. Flow cytometric analysis including various T cell memory and exhaustion/effector markers of $T_{ML/HCV}$ cells in rHCV (n = 5), cHCV and cured HCV targeting either conserved epitopes (AG; cHCV: n = 12, cured HCV: n = 7) or variant epitopes (ESC; cHCV: n = 8, cured HCV: n = 6). t-SNE representation with scaled expression depicted as color code (red: high; blue: low) **a**, representative dot plots (including control analyses of non-naïve and naïve bulk $CD8^+$ T cells) and bar charts (**b**; median fluorescence intensity (MFI) normalized to naïve $CD8^+$ T cells) are depicted. Bar charts show the median with IQR. Significance was assessed by Kruskal-Wallis test (one-sided) including Dunn's multiple comparisons test.

nature research

Corresponding author(s): Robert Thimme
Maike Hofmann

Last updated by author(s): Sep 27, 2020

Reporting Summary

Nature Research wishes to improve the reproducibility of the work that we publish. This form provides structure for consistency and transparency in reporting. For further information on Nature Research policies, see our Editorial Policies and the Editorial Policy Checklist.

Statistics

For all statistical analyses, confirm that the following items are present in the figure legend, table legend, main text, or Methods section.

n/a	Confirmed	
☐	☒	The exact sample size (*n*) for each experimental group/condition, given as a discrete number and unit of measurement
☐	☒	A statement on whether measurements were taken from distinct samples or whether the same sample was measured repeatedly
☐	☒	The statistical test(s) used AND whether they are one- or two-sided *Only common tests should be described solely by name; describe more complex techniques in the Methods section.*
☐	☒	A description of all covariates tested
☐	☒	A description of any assumptions or corrections, such as tests of normality and adjustment for multiple comparisons
☐	☒	A full description of the statistical parameters including central tendency (e.g. means) or other basic estimates (e.g. regression coefficient) AND variation (e.g. standard deviation) or associated estimates of uncertainty (e.g. confidence intervals)
☐	☒	For null hypothesis testing, the test statistic (e.g. *F*, *t*, *r*) with confidence intervals, effect sizes, degrees of freedom and *P* value noted *Give P values as exact values whenever suitable.*
☒	☐	For Bayesian analysis, information on the choice of priors and Markov chain Monte Carlo settings
☐	☒	For hierarchical and complex designs, identification of the appropriate level for tests and full reporting of outcomes
☐	☒	Estimates of effect sizes (e.g. Cohen's *d*, Pearson's *r*), indicating how they were calculated

Our web collection on statistics for biologists contains articles on many of the points above.

Software and code

Policy information about availability of computer code

Data collection: FACSDiva software

Data analysis	Multiparametric Flow cytometry data was analyzed using FlowJo software version 10.6.2 (Treestar, Becton Dickinson) and CyTOF workflow R package version 1.12.0. Visualization and statistical analysis was performed using GraphPad 8 software. Alignment of low input RNAseq analysis was performed using mapping tool STAR (version 2.5.2b). Reads were position sorted using SAMtools (version 1.6) 42. Duplicate read marking was performed using sambamba (version 0.6.5) 43 with 8 threads. BAM file indexes were generated using sambamba. Quality control was performed using the rnaseqc tool (version v1.1.8.1) 44 with the 1000 genomes assembly and gencode 19 gene models and no depth of coverage analysis, and also using samtools flagstat. Differential expression analysis was performed by the DESeq2 package. Gene set enrichment analysis (GSEA) was performed by the fgsea package by taking log2 fold change to rank genes. Gene Ontology and KEGG enrichment on the significantly differentially expressed genes were performed by the clusterProfiler package. Co-expression network analysis was performed by the WGCNA package 47. Consensus clustering was performed by the cola package. The ATC method was used to select feature genes and spherical k-means clustering was applied to partition samples. MiXCR version 2.1.12 48 was used to identify CDR3 clontypes from the individual FASTQ files of the RNAseq samples using the align and assemble commands with default options. These clonetypes were further analysed using Vdjtools version 1.19 for post analysis of TCR repertoires, using Java version 1.8.0_40 and R version 3.3.1. The MiXCR metadata file was initially converted and basic statistics and segment usage was evaluated using the CalcBasicStats and CalcSegmentUsage commands. After manual quality assurance, clonotype quantile statistics were calculated using the PlotQuantileStats command. Alignment of single-cell sequencing data was performed using bwa (version 0.6.2-r126) with default parameters. Clustering analysis and visualization were performed using the RaceID3 algorithm. Inter-patient heterogeneity was corrected using mnnCorrect function from the scran package implemented in the RaceID3. Dimensionality reduction for visualization was performed using the compfr function of RaceID3. Diffusion pseudotime (dpt) analysis on the cHCV dataset was performed using the destiny R package. The genes to be included in the dpt analysis were obtained using the getfdata function of RaceID3. Differential gene expression analysis was performed using the diffexpnb function of RaceID3 algorithm.

For manuscripts utilizing custom algorithms or software that are central to the research but not yet described in published literature, software must be made available to editors and reviewers. We strongly encourage code deposition in a community repository (e.g. GitHub). See the Nature Research guidelines for submitting code & software for further information.

Data

Policy information about availability of data

All manuscripts must include a data availability statement. This statement should provide the following information, where applicable:

- Accession codes, unique identifiers, or web links for publicly available datasets
- A list of figures that have associated raw data
- A description of any restrictions on data availability

The primary read files as well as expression count files for the single-cell RNA-sequencing datasets reported in this paper are available to download from GEO (accession number: GSE150305). The expression count files for the low input RNA sequencing are available to download from GEO (accession number: GSE150345). The raw data files for the low input RNA sequencing are available from EGA (accession number: EGAD00001006259). The gene sets used for gene set enrichment analysis: (i) exhaustion (chronic TCF-1-), memory-like (chronic TCF-1+) and memory signature (doi: 10.1016/j.immuni.2016.07.021), (ii) PD1int CD8 TILs signature (doi: 10.1053/j.gastro.2018.08.030) and for the TCF-1+ CD8 TILs signature (doi: 10.1016/j.immuni.2018.12.021). The remaining data supporting the findings of this study are available from the corresponding author upon request.

Field-specific reporting

Please select the one below that is the best fit for your research. If you are not sure, read the appropriate sections before making your selection.

☒ Life sciences ☐ Behavioural & social sciences ☐ Ecological, evolutionary & environmental sciences

For a reference copy of the document with all sections, see nature.com/documents/nr-reporting-summary-flat.pdf

Life sciences study design

All studies must disclose on these points even when the disclosure is negative.

Sample size	Patients were recruited and patient material was banked at the University Hospital Freiburg; inclusion criteria were:HLA-A02:01 or HLA-B27:05, HCV infection of genotype 1a or 1b, no liver cirrhosis, detectability of HCV-specific CD8+ T cells. Based on these criteria, samples of x patients were available for this study. This number is comparable to many other studies in the research field of human immunology and proved to be sufficient for the generation of reproducible results.
Data exclusions	For flow cytometric analysis, cell populations containing less than 5 cells were excluded. This data exclusion strategy has been applied and validated previously by our group to gain reproducible results in studies investigating virus-specific CD8+ T cells in human viral infections.
Replication	Analysis were performed in independent experiments. Independent experiments: scRNAseq analysis: 7 independent experiments; low-input RNAseq analysis: 4 independent experiments; flow cytometry analysis: 13 independent experiments.
Randomization	Patients were selected based on availability of samples to the selected time points of infection and detectability of virus-specific CD8+ T cells. Patients were grouped based on certain characteristics of their virus-specific CD8+ T cell response (e.g. targeting conserved versus variant epitopes) in combination with the clinical course (chronic versus cured versus spontaneously resolved). The study-relevant covariates HLA type, HCV genotype and cirrhosis was controlled by the inclusion criteria. The covariates age and gender are well-documented, e.g. median age of the chronic HCV cohort was 54.4 years and of the resolved HCV cohort 43.4 years. The gender ratio of the chronic HCV cohort was m/f: 20/18 and of the resolved HCV cohort m/f: 10/4.
Blinding	Blinding was not applied. Non-objective parameters were not included in the study design. Due to standardized analyses of the flow cytometric data set, biased analysis can be excluded.

Reporting for specific materials, systems and methods

We require information from authors about some types of materials, experimental systems and methods used in many studies. Here, indicate whether each material, system or method listed is relevant to your study. If you are not sure if a list item applies to your research, read the appropriate section before selecting a response.

Materials & experimental systems

n/a	Involved in the study
☐	☒ Antibodies
☒	☐ Eukaryotic cell lines
☒	☐ Palaeontology and archaeology
☒	☐ Animals and other organisms
☐	☒ Human research participants
☒	☐ Clinical data
☒	☐ Dual use research of concern

Methods

n/a	Involved in the study
☒	☐ ChIP-seq
☐	☒ Flow cytometry
☒	☐ MRI-based neuroimaging

Antibodies

Antibodies used

Bcl-2 , BioLegend , Cat No 658709 , clone 100 , Lot No B247324
CCR7 , BioLegend , Cat No 353232 , clone G043H7 , Lot No B278012
CCR7 , BioLegend , Cat No 353230 , clone G043H7 , Lot No B249691
CD127 , BioLegend , Cat No 351334 , clone A019D5 , Lot No B291922
CD127 , BioLegend , Cat No 351318 , clone A019D5 , Lot No B220642
CD28, BD, Cat No 555726, clone CD28.2, Lot No 9155648
CD39 , BioLegend , Cat No 328213 , clone A1 , Lot No B181300
CD45RA , BioLegend , Cat No 304142 , clone HI100 , Lot No B215533
PD-1 , BioLegend , Cat No 329920 , clone EH12.2H7 , Lot No B285220
PD-1 , BD , Cat No 563789 , clone EH12.1 , Lot No 9301566
TNF , BioLegend , Cat No 502930 , clone MAb11 , Lot No B263212
TNF , BD , Cat No 557647 , clone MAb11 , Lot No 7240562
CD137 , BD , Cat No 745737 , clone 4B4-1 , Lot No 833516
CD45RA , BD , Cat No 564442 , clone HI100 , Lot No 7075872
CD8 , BD , Cat No 564804 , clone RPA-T8 , Lot No 9196503
CD8 , BD , Cat No 555367 , clone RPA-T8 , Lot No 9343893
CD8 , BD , Cat No 564526 , clone RPA-T8 , Lot No 8143569
IFNɣ , BD , Cat No , clone 25723.11 , Lot No 9262323
CD14 , eBioscience , Cat No 47-0149-42 , clone 61D3 , Lot No 2055188
CD19 , eBioscience , Cat No 47-0199 , clone HIB19 , Lot No 2010169
CD38 , eBioscience , Cat No 25-0388 , clone HB7 , Lot No 1918569
IRF4 , eBioscience , Cat No 61-9858-82 , clone 3E4 , Lot No 4301670
TOX1 , eBioscience , Cat No 50-6502 , clone TRX10 , Lot No 4291379
Eomes, eBioscience, Cat No 46-4877-42, clone WD1928, Lot No 2016453
T-bet, eBioscience, Cat No 25-5825-82, clone 4B10, Lot No 1995491
TCF-1 , Cell signaling , Cat No #6444 , clone C63D9 Lot No 8

Validation

standardized analysis in different cohorts, antibody titration on PBMCs including unstained controls, comparisons of different antibody clones and conjugates and validated by publications:
Bcl-2 , clone 100: antibody titration on PBMCs; validated with respect to differential expression of naïve and non-naïve T cell subpopulations
CCR7, clone G043H7: antibody titration on PBMCs; control clones 150503 and 3D12; validated with respect to differential expression of naïve and non-naïve T cell subpopulations
CD127 , clone A019D5: antibody titration on PBMCs; control clone HIL-7R-M21; validated with respect to differential expression of naïve and non-naïve T cell subpopulations
CD28,clone CD28.2: antibody titration on PBMCs; control clone B-T3; validated with respect to differential expression of naïve and non-naïve T cell subpopulations
CD39, clone A1: antibody titration on PBMCs; control clone TU66; validated with respect to differential expression of naïve and non-naïve T cell subpopulations
CD45RA, clone HI100: antibody titration on PBMCs; validated with respect to differential expression of naïve and non-naïve T cell subpopulations
PD-1, clone EH12.2H7: antibody titration on PBMCs; control clones eBioJ105 and EH12.1; validated with respect to differential expression of naïve and non-naïve T cell subpopulations
PD-1, clone EH12.1: antibody titration on PBMCs; control clones eBioJ105 and EH12.2H7; validated with respect to differential expression of naïve and non-naïve T cell subpopulations
TNF, clone MAb11: antibody titration on PBMCs; validated with respect to differential expression of activated and non-activated T cell subpopulations
CD137, clone 4B4-1: antibody titration on PBMCs; validated with respect to differential expression of naïve and non-naïve T cell subpopulations
CD8, clone RPA-T8: antibody titration on PBMCs; control clones GHI/75 and SK1; using B cells as negative control

IFNɣ, clone 25723.11: antibody titration on PBMCs; control clone 4S.B3; validated with respect to differential expression of activated and non-activated T cell subpopulations
CD14 , clone 61D3: antibody titration on PBMCs; control clones M5E2 and MϕP9; using T cell populations as negative control
CD19, clone HIB19: antibody titration on PBMCs; control clone SJ25C1; using T cell populations as negative control
CD38, clone HB7: antibody titration on PBMCs; control clone HIT2; validated with respect to differential expression of naïve and non-naïve T cell subpopulations
IRF4, clone 3E4: antibody titration on PBMCs; validated with respect to differential expression of naïve and non-naïve T cell subpopulations
TOX1, clone TRX10: antibody titration on PBMCs; control clone REA473; validated with respect to differential expression of naïve and non-naïve T cell subpopulations
Eomes, clone WD1928: antibody titration on PBMCs; validated with respect to differential expression of naïve and non-naïve T cell subpopulations
T-bet, clone 4B10: antibody titration on PBMCs; control clones O4-46; validated with respect to differential expression of naïve and non-naïve T cell subpopulations
TCF-1, clone C63D9: antibody titration on PBMCs; control clone 7F11A10; validated with respect to differential expression of naïve and non-naïve T cell subpopulations

Human research participants

Policy information about studies involving human research participants

Population characteristics	Patients with HCV infection (chronic/resolved; genotype 1a or 1b), without liver cirrhosis and carrying HLA-A02:01 or HLA-B27:05 were recruited at the University Hospital Freiburg. Median age of the chronic HCV cohort was 54.4 years and of the resolved HCV cohort 43.4 years. The gender ratio of the chronic HCV cohort was m/f: 20/18 and of the resolved HCV cohort m/f: 10/4
Recruitment	Patients suffering from HCV infection were recruited at the University Hospital Freiburg, samples were banked and retrospectively selected according to the following inclusion criteria: HLA-A02:01 or HLA-B27:05, HCV infection of genotype 1a or 1b, no liver cirrhosis, detectability of HCV-specific CD8+ T cells
Ethics oversight	Ethic Commitee of Albert-Ludwig-Universität, Freiburg, Germany; 474/14; 275/15; 516/19

Note that full information on the approval of the study protocol must also be provided in the manuscript.

Flow Cytometry

Plots

Confirm that:

☒ The axis labels state the marker and fluorochrome used (e.g. CD4-FITC).

☒ The axis scales are clearly visible. Include numbers along axes only for bottom left plot of group (a 'group' is an analysis of identical markers).

☒ All plots are contour plots with outliers or pseudocolor plots.

☒ A numerical value for number of cells or percentage (with statistics) is provided.

Methodology

Sample preparation	PBMCs from EDTA-anticoagulated patient blood were isolated by density gradient centrifugation using Pancoll and crypopreserved upon use. Cryopreserved isolated human PBMCs were thawed in complete RPMI media and prepared for multiparametric flow cytometry analysis (including magnetic bead-based enrichment of antigen-specific CD8+ T cells), in vitro expansion or FACS sorting for following low-input and single-cell RNA sequencing analysis.
Instrument	FACSCanto II, LSRFortessa, FACSMelody (BD)
Software	FlowJo_v10.6.2 (Treestar), cytofWorkflow R package version 1.12.0
Cell population abundance	Abundance of HCV-specific CD8+ T cells are very low (<0.1 %)
Gating strategy	Lymphocytes gated on FSC-A and SSC-A, Doublet exclusion on FSC-A and FSC-H and FSC-A and FSC-W, Exclusion of dead cells, B cells and monocytes, Gating on CD8+ cells, Exclusion of naive cells (CCR7+CD45RA+), Gating of HCV-specific CD8+ T cells via p-MHC-I tetramers, Gating on CD127+PD-1+ (ML), CD127-PD-1+ (TE), CD127+PD-1- (M) or CD127hi, CD127int and CD127lo HCV-specific CD8+ T cells.

☒ Tick this box to confirm that a figure exemplifying the gating strategy is provided in the Supplementary Information.